ISPRS Journal of Photogrammetry and Remote Sensing 167 (2020) 345–362

Contents lists available at ScienceDirect

ISPRS Journal of Photogrammetry and Remote Sensing

journal homepage: www.elsevier.com/locate/isprsjprs

Detection of radioactive waste sites in the Chornobyl exclusion zone using UAV-based lidar data and multispectral imagery

S. Briechle[a,*], N. Molitor[b], P. Krzystek[a], G. Vosselman[c]

[a] Munich University of Applied Sciences, Munich, Germany
[b] Plejades GmbH, Griesheim, Germany
[c] Faculty of Geo-Information Science and Earth Observation (ITC), University of Twente, Enschede, the Netherlands

ARTICLE INFO

Keywords:
UAV
Lidar
Multispectral imagery
Radioactive waste sites
3D vegetation mapping
Machine learning

ABSTRACT

The severe accident at the Chornobyl Nuclear Power Plant (ChNPP) in 1986 resulted in extraordinary contamination of the surrounding territory, which necessitated the creation of the Chornobyl Exclusion Zone (ChEZ). During the accident, liquidation materials contaminated by radioactive fallout (e.g., contaminated soil and trees) were buried in so-called Radioactive Waste Temporary Storage Places (RWTSPs). The exact locations of these burials were not always sufficiently documented. However, for safety management, including eventual remediation works, it is crucial to know their locations and rely on precise hazard maps. Over the past 34 years, most of these so-called trenches and clamps have been exposed to natural processes. In addition to settlement and erosion, they have been overgrown with dense vegetation. To date, more than 700 burials have been thoroughly investigated, but a large number of burial sites (approximately 300) are still unknown. In the past, numerous burials were identified based on settlement or elevation in the decimeter range, and vegetation anomalies that tend to appear in the immediate vicinity. Nevertheless, conventional detection methods are time-, effort- and radiation dose-intensive. Airborne gamma spectrometry and visual ground inspection of morphology and vegetation can provide useful complementary information, but it is insufficient for precisely localizing unknown burial sites in many cases. Therefore, sensor technologies, such as UAV-based lidar and multispectral imagery, have been identified as potential alternative solutions. This paper presents a novel method to detect radioactive waste sites based on a set of prominent features generated from high-resolution remote sensing data in combination with a random forest (RF) classifier. Initially, we generate a digital terrain model (DTM) and 3D vegetation map from the data and derive tree-based features, including tree density, tree height, and tree species. Feature subsets compiled from normalized DTM height, fast point feature histograms (FPFH), and lidar metrics are then incorporated. Next, an RF classifier is trained on reference areas defined by visual interpretation of the DTM grid. A backward feature selection strategy reduces the feature space significantly and avoids overfitting. Feature relevance assessment clearly demonstrates that the members of all feature subsets represent a final list of the most prominent features. For three representative study areas, the mean overall accuracy (OA) is 98.2% when using area-wide test data. Cohens' kappa coefficient κ ranges from 0.609 to 0.758. Additionally, we demonstrate the transferability of a trained classifier to an adjacent study area (OA = 93.6%, κ = 0.452). As expected, when utilizing the classifier on geometrically incorrect and incomplete reference data, which were generated from old maps and orthophotos based on visual inspection, the OA decreases significantly to 65.1% (κ = 0.481). Finally, detection is verified through 38 borings that successfully confirm the existence of previously unknown buried nuclear materials in classified areas. These results demonstrate that the proposed methodology is applicable to detecting area-wide unknown radioactive biomass burials in the ChEZ.

1. Introduction

On April 26, 1986, an explosion of Reactor Unit 4 at the Chornobyl Nuclear Power Plant (ChNPP), located approximately 100 km north of Kiev, Ukraine, was recorded as a major accident according to the International Nuclear and Radiological Event Scale. To re-establish safety, the surrounding population was evacuated from severely affected areas, and the Chornobyl Exclusion Zone (ChEZ) was created.

* Corresponding author.
E-mail addresses: sebastian.briechle@hm.edu (S. Briechle), norbertmolitor@pleja.de (N. Molitor), peter.krzystek@hm.edu (P. Krzystek), george.vosselman@utwente.nl (G. Vosselman).

https://doi.org/10.1016/j.isprsjprs.2020.06.015
Received 18 November 2019; Received in revised form 27 May 2020; Accepted 18 June 2020
Available online 01 August 2020

This zone remains in effect today. Based on the extraordinary contamination caused by the spread of radioactive materials, the forest in the fallout trails adjacent to the ChNPP turned reddish-brown and died (hereafter referred to as the "Red Forest"). During the implementation of liquidation measures, the contaminated biomass and topsoil were buried on-site in trenches and clamps, then covered by a clean soil layer with a typical thickness of approximately 1 m. These burials were created in areas called Radioactive Waste Temporary Storage Places (RWTSPs). A total of nine RWTSPs were created in the vicinity of the ChNPP, consisting of approximately 1000 trenches and clamps (Molitor et al., 2017). To stabilize the surface cover and reduce re-suspension of contaminated dust particles by wind, many parts of the RWTSPs were re-vegetated. Initially, clean-up actions decreased the external exposure dose rate significantly. However, based on the absence of appropriate barriers, burials in RWTSPs do not provide sufficient protection against radiation mobilization into groundwater. Unfortunately, accident liquidation measures were performed under extraordinary boundary conditions. Therefore, no detailed systematic documentation of the RWTSPs is available. Most current information relies on improvised records that were created during or after the liquidation measures. Thus, a comprehensive overview and precise mapping of trenches and clamps (exact number, location, geometry, contents, etc.) are necessary to improve safety during maintenance and facilitate the eventual remediation of burials.

The main objective of this study is to map unknown radioactive biomass burials in the ChEZ automatically and accurately. On-site visual inspections of known burials revealed three important facts. First, many burials can be identified based on settlement or elevation in the decimeter range or more. Second, distinctive vegetation features are also characteristic of many burials. Third, based on significant remaining contamination, a remote measurement technique is required to avoid risky trespassing of the study areas. Therefore, the key idea of this study is to utilize remote sensing devices in combination with machine learning (ML) methods to perform precise 3D vegetation mapping followed by the classification of areas containing buried radioactive materials. As a sensor platform, a UAV can be deployed to collect data from a safe distance. Because it is able to penetrate vegetation, airborne lidar data can be utilized to extract precise digital terrain models (DTMs), even in overgrown areas (Sithole and Vosselman, 2004; Gevaert et al., 2018). By combining DTM information with standard ML techniques, the detection of small terrain height anomalies has been performed successfully in the past. By inspecting small elevation changes, cultural remains can be identified in archaeological investigations (Lasaponara et al., 2010; Bollandsås et al., 2012), even when they are located under dense vegetation (Guyot et al., 2018). Furthermore, lidar facilitates precise 3D mapping of forests at the tree level (Reitberger et al., 2008). Because multispectral (MS) imagery can support tree species classification (Holmgren et al., 2008; Trier et al., 2018), we supplemented the lidar sensor with two high-resolution MS cameras to collect image data in the visible and near-infrared (NIR) spectra.

The current paper proposes the utilization of terrain-based and vegetation-based features in combination with a random forest (RF) classifier for the area-wide detection of unknown radioactive waste sites in the ChEZ. Using UAV-based lidar data and MS imagery, we conduct a precise 3D vegetation mapping at the tree level and introduce novel tree-based features (*TF*). Subsequently, we train an RF classifier to predict the class labels for each DTM grid point ("trench", "clamp", "non-contaminated"). Excellent classification results are achieved, and a backward feature selection strategy demonstrates that e.g. *TF* and fast point feature histograms (FPFH) can enhance the proposed classifier. Our results are verified by 38 borings that confirm the existence and absence of previously unknown buried nuclear materials in the classified areas (OA = 89.5%). Interestingly, at an average depth of 1–2 m, the borings hit radioactive material, exhibiting dose rates that were up to 30 times greater than those on the terrain surface. Finally, the existing hazard maps have been upgraded to minimize worker radiation dose uptake and optimize accident liquidation.

In the following sections, we address related work, the study areas, reference data, the UAV system, sensors, and data preprocessing. Subsequently, we present the entire processing pipeline for the detection of radioactive burials and the conducted experiments, including sensitivity analysis. Finally, we discuss the results and draw conclusions from our research.

2. Related work

2.1. Risk management in the ChEZ

An EU-financed project entitled "Support to radioactive waste management in Ukraine" (European Union, 2014) facilitated numerous research studies, including the investigation on radioactive waste sites. Some RWTSPs have already been thoroughly investigated, but an estimated 300 burial sites remain unknown in terms of their exact location and geometry. These sites must be identified and characterized. Because ground dose rate measurements and electromagnetic soil conductivity surveys were not expedient, Bugai et al. (2005) successfully carried out ground-based geo-radar surveys using ground-penetrating radar (GPR). Using this technique, the subsurface geometry of one suspected burial site was elucidated. Based on a GPR survey, Saintenoy et al. (2017) verified the position of a trench in the RWTSP Red Forest. However, such ground-based methods necessitate considerable radiation exposure for workers. Furthermore, the GPR approach is relatively time consuming for the exploration of larger vegetated areas that are difficult to access. Zabulonov et al. (2015) conducted UAV-based geophysical surveys using a gamma spectrometer. By detecting local inhomogeneity in spectrometer data, the authors revealed that the accurate mapping of burials located in non-vegetated areas is possible using high-resolution gamma field radiation measurements (detection rate = 90%). The results demonstrated that local gamma ray intensity significantly exceeds the level of the total background radiation in contaminated areas. However, in vegetated areas, biomass substantially distorts measurements and the detection rate drops significantly to 50%. Recently, there has been increased pressure to make the ChEZ accessible again. To this end, simulations have been carried out to model worker radiation dose uptakes (Molitor et al., 2017). Nevertheless, improved models are needed to create action plans for forest maintenance and mitigate hazard situations – such as forest fires and tornadoes – more efficiently. Therefore, simulations must consider the individual radioactive radiation levels of different tree species to achieve the most realistic possible results.

2.2. Vegetation anomalies in the ChEZ

In the ChEZ, various studies have been carried out to explore the impact of radioactive contamination on the vegetation. Because the half-lives of 137-Cs and 90-Sr are approximately 30 years (Flynn et al., 1965), these radioactive isotopes still exist in the soil of contaminated areas and have been absorbed by the vegetation. Bugai et al. (2012) characterized the hydro-geological situation in the ChEZ and modeled groundwater transport to describe the migration of radionuclides. Furthermore, Kashparov et al. (2012) presented studies describing the biogenic migration of radionuclides from subsurface storage to plants. Moreover, Thiry et al. (2009) demonstrated that trees growing on burial sites accumulated an average of 1.7 times more 137-Cs and 5.4 times more 90-Sr in their above-ground biomass compared to trees growing off of burial sites. In a long-term observation, Arkhipov et al. (1994) explored the forest stands regarding viability and mortality rate, re-establishment and canopy growth, and reproduction anomalies. Their results show that these parameters depend on the absorbed irradiation dose, on the age of the tree stand, and on forest composition. Moreover, Yoschenko et al. (2011) investigated over 1100 replanted Scots pines

selected from areas with strongly varying levels of radioactive contamination. The authors reported on the effects occurring on the morphological level of trees that were exposed to chronic radiation. Based on long-term studies, Tikhomirov and Shcheglov (1994) revealed that the migration of radionuclides is highly dependent on the tree species. Furthermore, the authors found out that coniferous trees are on average an order of magnitude less resistant to radioactive contamination than deciduous trees. According to Davids and Tyler (2003), spectral reflectance measurements of silver birch and Scots pine can be used to detect the effect of radionuclide contamination on the vegetation. Particularly, the authors demonstrated that certain spectral characteristics of leaves and needles correlate well with the level of radioactive contamination. All in all, vegetation anomalies (e.g., tree density, dominant tree species, tree shape, spectral reflectance of the vegetation, etc.) tend to appear in highly contaminated areas such as the vicinity of trenches and clamps.

2.3. Vegetation mapping

In the past, extensive research has been conducted on vegetation mapping using remote sensing data, particularly airborne laser scanning (ALS) point clouds fused with optical imagery (Latifi and Heurich, 2019). One major research focus was to establish methods that would work at the tree level. A delineation of single trees from ALS data was either performed based on a previously generated canopy height model (Pyysalo and Hyyppå, 2002; Solberg et al., 2006) or on the original 3D point cloud (Reitberger et al., 2009; Wu et al., 2016). For the classification of individual tree species, a large majority of previous studies relied on a two-step approach (Fassnacht et al., 2016). First, handcrafted feature sets describing the geometry and radiometry of single trees were extracted from the data. Second, appropriate ML classifiers were applied to categorize the single trees. For example, Yu et al. (2017) classified three tree species using multispectral ALS data (OA = 86%). Moreover, Shi et al. (2018a) categorized five species, fusing ALS data and hyperspectral imagery (OA = 84%). Based on the features generated from ALS data and color-infrared imagery, Kaminska et al. (2018) classified six tree classes (OA = 94%). Recently, Amiri et al. (2019) reported on a combined classification of tree species and standing dead trees with crowns (OA = 82%). Overall, these studies motivated the generation of handcrafted features for an RF-based classification of individual tree species in the ChEZ.

3. Materials

3.1. Study areas

In this paper, experimental results for three different study areas with a total area of 37 ha are presented (Fig. 1). Located approximately 1.5 km west of the ChNPP, these areas are situated in the RWTSP Red Forest and RWTSP Yanov Station areas. For these areas, a historical map created from the memories of so-called liquidation workers indicated the existance of possible radioactive waste sites (Fig. 2). In a first UAV flight mission conducted in November of 2017, area#1 (6 ha) was surveyed using a YellowScan Mapper I laser scanner (Briechle et al., 2018). The lidar data were supplemented with MS images captured in a second mission in April of 2018. At the same time, both lidar data and MS images were collected in area#2 (8 ha) and area#3 (23 ha). With a tree density of approximately 400 trees/ha, all three study areas are densely vegetated. The main tree species are Scots pine (*Pinus sylvestris*), silver birch (*Betula pendula*), and black alder (*Alnus glutinosa*) with tree heights of up to 30 m (Bonzom et al., 2016). Overall, the forest stand was found to be dominated by Scots pine planted after the nuclear disaster, comprising approximately 50% of all trees. Based on visual interpretation of aerial imagery, we roughly estimated the distribution of pines, birches, and alders in area#1 (50/20/30), area#2 (40/30/30), and area#3 (60/20/20).

3.2. Reference data

3.2.1. Visual interpretation

For obvious reasons, the ground truth data for tree species classification could not be acquired by field measurements. Thus, the reference dataset was prepared manually and balanced according to the three occurring tree species (pine, birch, alder). Based on visual interpretation of the generated orthomosaics and 3D geometries of single trees, we labeled 684 tree segments (228 per tree species). Thereafter, for each study area, these reference datasets were randomly split into training and test datasets using a sample ratio of 0.8.

Reference data for trenches and clamps were only available in area#3, using RWTSP vector data. These data were digitized from old maps and orthophotos based on visual inspection in the past using a simple office scanner and uncalibrated digital cameras. Therefore, the data are geometrically incomplete and show random position offsets in the order of a few meters. This can be clearly observed by overlaying the reference data and the normalized DTM height, which was generated from the ALS data (Fig. 3). Nevertheless, we used this rather inappropriate dataset in the labeling process for one of our experiments. In all other experiments, we relied on manually labeled reference data created by visual interpretation of the normalized DTM. In area#1 and area#2, the structure of burials was quite obvious and labeling was straightforward. However, in area#3, the labeling was more challenging because of fairly nonsystematic DTM structures. Here, the directions and lengths of the burials were partially unclear. Although the labeling was supported by RWTSP vector data, the reference dataset in this study area must be considered less reliable. For the labeling of DTM grid pixels, we outlined polygons representing 25 trenches and eight

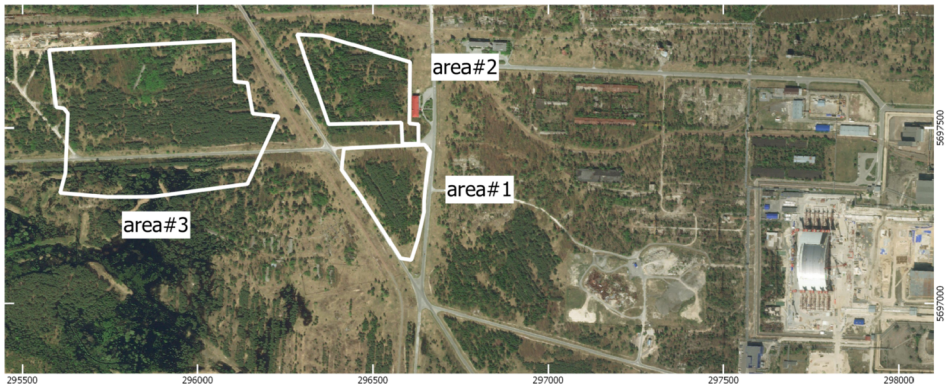

Fig. 1. Overview of the study areas, located around 1.5 km west of Reactor Unit 4 at the ChNPP; Coordinate system: UTM zone 36N (EPSG 32636); Base map source: bing map ©Microsoft Corporation.

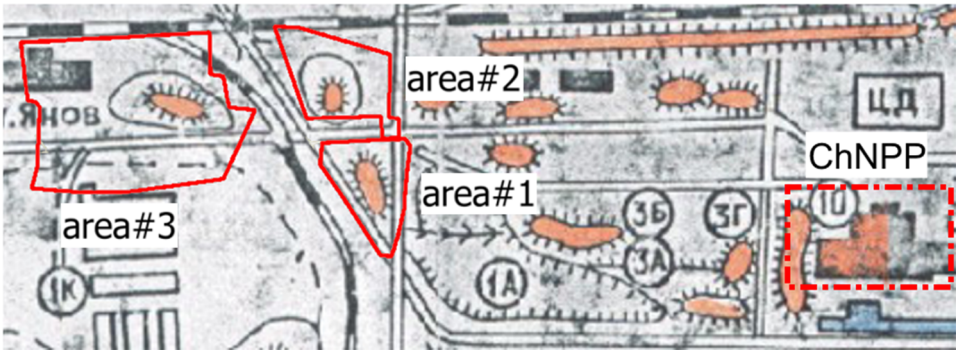

Fig. 2. Scan of a historical map that was created from the memories of liquidators, roughly showing positions and extents of burials (Antropov et al., 2001); outlines of study areas in red. (For interpretation of the references to color in this figure legend, the reader is referred to the web version of this article.)

clamps from all three study areas, covering an area of 9116 m^2 and 2900 m^2, respectively. Using a 50 cm DTM, more than 48,000 samples were extracted from these burials. Additionally, samples for non-contaminated DTM pixels were selected some meters off the burials to guarantee the pureness of samples. Then, for each study area, we utilized a sample ratio of 0.5 to randomly split the reference data into training and test datasets. Subsequently, the particular test datasets were completed by considering all remaining unlabeled pixels in the corresponding study areas as non-contaminated. As a consequence, the quality of the classifier could be tested area-wide and, especially in the transition zones from burials to non-contaminated areas.

3.2.2. Ground reference data

In preceding ground surveys, neither a visual interpretation of the terrain nor anomalies in the equivalent dose rate (EDR) measurements on the ground surface ($EDR_{surface}$) indicated existing trenches. However, a strong evidence was provided based on the detection methods described in this paper. Therefore, during an evaluation campaign conducted in autumn 2018, 20 on-site borings were drilled directly into the suspected trenches of area#1 and nine in area#2. For comparison, nine additional borings were drilled at a considerable distance of at least 15 m away from the expected trenches of area#1 (Table 3). Borings C1, C2, C3, C4 and C5 were planned at spots showing unexceptional $EDR_{surface}$ values. In contrast, the locations for borings C98, C206, C208 and C216 were selected in places showing relatively high $EDR_{surface}$ values, thus assuming they were suspicious for buried contaminated waste. In area#3, no borings have been conducted so far. In general, all borings were performed by the Central Radioactive Waste Management Enterprise (CRWME), a state organisation responsible for maintenance and management of the RWTSPs under authority of the State Agency of Ukraine for the Exclusion Zone Management. The borings were carried out using a gasoline motor drill (up to a depth of 1.5 m) and a Geolog-2 hand drill (depth 1.5–2.5 m). The EDR was measured on the ground surface and inside the bore holes using an MKS-07 “Poshuk” dosimeter-radiometer. Tables 1–3 show $EDR_{surface}$ values, maximum EDR values (EDR_{max}) and the corresponding depth for each boring. Ratio $\frac{EDR_{max}}{EDR_{surface}}$ is a coefficient to demonstrate the degree of contamination inside the borings compared to the ground surface.

3.3. UAV system

UAV-based sensor systems operate at a sufficient safe distance,

Fig. 3. Available RWTSP reference data and manually labeled reference data in area#3, showing possible trenches/clamps and normalized DTM height. (base map: bing map ©Microsoft Corporation).

Table 1
Borings in suspected trenches of area#1.

Boring ID	$EDR_{surface}$ [µSv/h]	EDR_{max} [µSv/h]	Depth for EDR_{max} [m]	$\frac{EDR_{max}}{EDR_{surface}}$
111	1.5	13.4	1.8	8.9
112	1.0	7.2	0.8	7.2
113	0.4	13.5	1.4	33.8
114	1.9	7.6	0.6	4.0
115	1.6	14.6	1.0	9.1
121	1.0	20.3	1.4	20.3
122	1.6	7.7	1.2	4.8
123	1.9	14.3	1.2	7.5
124	0.9	26.5	1.4	29.4
125	0.8	24.5	1.8	30.6
131	1.3	2.4	0.8	1.9
132	0.7	7.0	1.0	10.3
133	0.9	8.6	1.2	9.2
134	2.9	4.1	0.8	1.4
135	1.9	8.3	0.8	4.4
151	3.8	16.3	1.2	4.3
152	1.0	18.6	1.2	18.6
153	2.9	17.5	0.6	6.0
154	1.3	7.3	1.6	5.6
155	1.5	10.3	1.2	6.9

Table 2
Borings in suspected trenches of area#2.

Boring ID	$EDR_{surface}$ [µSv/h]	EDR_{max} [µSv/h]	Depth for EDR_{max} [m]	$\frac{EDR_{max}}{EDR_{surface}}$
211	0.7	6.0	1.6	8.6
221	1.5	10.1	1.4	6.7
222	1.0	30.2	1.6	30.2
232	2.4	10.3	0.6	4.3
233	2.9	12.3	1.0	4.2
234	0.6	12.8	1.2	21.3
242	1.5	18.8	1.0	12.5
243	4.7	14.9	1.4	3.2
244	1.3	20.2	1.6	15.5

Table 3
Borings drilled at a considerable distance away from the trenches of area#1.

Boring ID	$EDR_{surface}$ [µSv/h]	EDR_{max} [µSv/h]	Depth for EDR_{max} [m]	$\frac{EDR_{max}}{EDR_{surface}}$
C1	1.3	1.3	0.0	1.0
C2	3.2	3.2	0.0	1.0
C3	3.9	3.9	0.0	1.0
C4	1.0	1.0	0.0	1.0
C5	0.6	0.6	0.0	1.0
C198	10.8	10.8	0.0	1.0
C206	7.5	7.5	0.0	1.0
C208	8.0	8.0	0.0	1.0
C216	4.8	6.7	0.2	1.4

which is of prime importance considering the high radiation dose rates within the study area. For our flight missions, we utilized an octocopter that was developed by a team from the Department of Nuclear Physics Technologies of the Institute of Environment Geochemistry of the National Academy of Sciences of Ukraine. With a maximum payload of 5 kg, both the lidar system and the MS cameras can be carried by the octocopter simultaneously (Fig. 4). Nevertheless, we relied on a separate configuration, mainly to maximize lidar mission time. Regarding

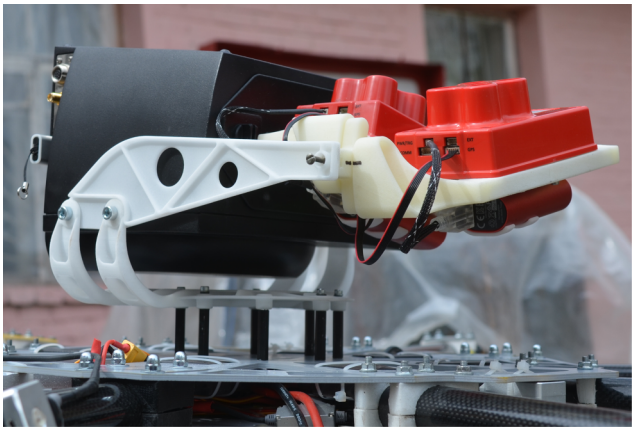

Fig. 4. UAV-mounted laserscanner and multispectral cameras.

safety issues, the pilots had to ensure a minimum distance from the ChNPP of 1 km. Moreover, no power lines were flown over to avoid possible electromagnetic interaction with Global Navigation Satellite System (GNSS) signals and radio link. All flights were carried out in fully automatic mode to avoid the direct trespassing of contaminated areas. Advantageously, local authorities allowed flying the UAV out of visual line of sight. To avoid collisions, the relative altitude in mapping mode was set to at least 50 m in this flat terrain, guaranteeing a safety distance of approximately 20 m to the highest tree crowns. Furthermore, the safety distance for operator at take-off and landing was approximately 15 m. Finally, all data presented in this paper were collected during sunny, partly cloudy weather conditions at a mostly constant wind speed (2–3 m/s).

3.4. Lidar data

Lidar data were collected by a YellowScan Mapper I laser scanner (Table 4). Flights were conducted at a constant altitude of 50 m and speed of 6 m/s. Therefore, the relatively slow speed of the copter enabled a high lidar point density, which is important for a sufficient penetration rate to the ground to ensure the generation of detailed DTMs. The maximum lidar mission time with one battery set was approximately 20 min. GNSS waypoints were defined in the flight plans to guarantee parallel flight lines and a constant line-to-line distance of 40 m. During a one-week mission in the ChEZ in April of 2018, five leaf-off lidar flights were conducted in three selected areas. More flights were not possible due to upcoming wind speeds up to 20 m/s. A calibration flight over a building was conducted on the first day to check the boresight angles provided by the manufacturer. Simultaneously to all UAV flights, GNSS measurements were collected by a Trimble R4 base station (measurement rate: 1 s). These data were used in a differential GNSS postprocessing step using the commercial software

Table 4
Technical specifications of the YellowScan Mapper I laserscanner (YellowScan, 2016).

Item	Value
Laser wavelength	905 nm
Pulse rate	18.5 kHz
Echoes per shot	3 (first, middle, last return)
Weight	2.1 kg (battery included)
Range resolution	4 cm
Precision[1]	10 cm
Absolute (XY) accuracy[2]	0.10 m + 1% of altitude
Absolute (Z) accuracy	0.10 m + 0.5% of altitude

[1]Also called reproducibility or repeatability (variation of measurements taken on the same target).
[2]Degree of conformity of a measured position to its actual (true) value.

Inertial Explorer 8.70 (NovAtel Inc., 2017) to ensure flight trajectories with centimeter-level precision. Following the flight missions, the scan angle range of the lidar data was reduced from 100° to 70° to eliminate potentially inaccurate long-distance measurements on the edges of strips, resulting in a nominal point density of approximately 53 points/m^2 (effective side lap of 43%). For the following lidar preprocessing steps, we utilized BayesStripAlign 1.3 (BayesMap Solutions LLC, 2018). The boresight angle differences were calculated using the "calib" option and the strips of the aforementioned calibration flight. The residuals amounted to 0.02° (roll), −0.12° (pitch), and −0.12° (yaw) and were subsequently used to correct all recorded flight strips ("corr" option). Next, all strips were aligned to achieve geometrically consistent lidar point clouds. Note that the "align" option in BayesStripAlign 1.3 is based on the approach discussed in Jalobeanu and Gonçalves (2014). Overall, the mean discrepancy between adjacent strips was approximately 5 cm, which is in the range of the measurement accuracy of the lidar instrument. By fitting the ALS point clouds to the enclosing polygons of nearby buildings ("shift" option), absolute 3D georeferencing with an accuracy of a few centimeters was achieved.

3.5. MS imagery

We captured MS images using two MicaSense RedEdge cameras (Table 5) with a total payload of 500 g, incl. external batteries. These MS cameras capture light wavelengths in five spectral bands between 475 nm and 840 nm. The two cameras were mounted in a twisted configuration with an angle of 22.5°. This setup guaranteed a 50% side overlap of the camera foot-prints and a total field of view of approximately 70°. Time synchronization of the cameras was realized by recording images with a frame rate of 2 s at each even GPS second. During data collection, the altitude was 130 m, leading to a ground sample distance of 8.9 cm/pixel. A flight speed of 9 m/s accounted for a forward overlap of 79%, whereas the lateral overlap was set to 50%. To compensate for changing illumination conditions during and between the flights, we utilized both MicaSense's calibrated reflectance panel (CRP) and downwelling light sensor (DLS). Basically, these accessories are able to provide useful information for the subsequent reflectance calibration. In practice, we took close-up images of the CRP before and after each flight. Moreover, the DLS was installed on top of the UAV, facing upwards with a clear view of the sky. Before each flight, we checked the calibration of the DLS magnetometer to ensure correct heading and orientation measurements. Agisoft PhotoScan Professional 1.4.1 (Agisoft LLC, 2018) was used for the following postprocessing steps. Initially, all images were aligned area-wise in a bundle adjustment (option "highest"). Here, the implemented RedEdge camera model was based on a standard frame camera model. In detail, the model specifies the transformation from point coordinates in the local camera coordinate system to the pixel coordinates in the image frame. Overall, the model comprises focal length, principal point offsets, two radial and two tangential distortion coefficients, and two skewness coefficients. In our approach, we estimated the master and slave camera models for the first flight and applied it to all other flights. The mean reprojection error for all flights was 1.3 pixels, corroborating our assumption of constant camera parameters between flights. Finally, dense photogrammetric 3D point clouds were generated with a point density of approximately 80 points/m^2 (option "high").

Table 5
Technical specifications of the MicaSense RedEdge multispectral camera (MicaSense Inc, 2015).

Item	Value
Focal length	5.5 mm
Field of view	47.2° horizontal, 69.7° horizontal (double-camera setup), 35.4° vertical
Imager size / resolution	4.8 mm × 3.6 mm / 1280 × 960 pixels
Spectral bands	Blue (475 nm), Green (560 nm), Red (668 nm), Red Edge (717 nm), Near IR (840 nm)

4. Methodology

4.1. Outline of the proposed method

Initially, various pre-processing steps must be performed for detecting radioactive waste sites. First, the reflectance of the 2D aerial images was calibrated, and Normalized Difference Vegetation Index (NDVI) and Red Edge Normalized Difference Vegetation Index (RENDVI) orthomosaics were created. Previous studies have proven a positive effect on the results for tree species classification by normalizing lidar intensity values (Höfle and Pfeifer, 2007; Korpela et al., 2010; Ørka et al., 2012). Thus, in our approach, the radiometric information of all lidar points was adjusted in a data-driven correction step. Based on the resulting lidar point cloud, ground points were filtered and a regular DTM grid was computed. Next, the lidar point cloud was segmented into 3D clusters representing single trees using the normalized cut algorithm (Reitberger et al., 2009). The convex hulls of the segmented trees were then projected onto the orthomosaics to extract NDVI and RENDVI features for each segment. To supplement the geometric and radiometric features generated from the lidar point clouds of single tree segments, tree species classification was conducted based on a standard RF classifier including a feature selection step. Based on the results of tree classification, tree-based features (*TF*) were generated to describe possible vegetation anomalies. Next, the normalized DTM height (h_{norm}) was extracted from the DTM grid. In combination with lidar metrics (*LM*) and *FPFH*, an RF classifier was trained to distinguish burial sites (trenches and clamps) from non-contaminated areas. In a recursive feature elimination step, the most significant features were identified. Finally, probability maps and enclosing 2D polygons for burial sites were generated. The entire processing pipeline is illustrated in Fig. 5. In the following sections, all important steps are described in greater detail.

4.2. Pre-processing of sensor data

4.2.1. Reflectance calibration of MS imagery

MS imagery was captured at changing light conditions over different days and times (see Section 3.5). Therefore, the reflectance must be calibrated to generate high-quality images. We performed this step in Agisoft PhotoScan Professional 1.4.1, integrating the spectral information from both the CRP and DLS. Initially, panel-specific absolute reflectance values for the spectral range of the camera were introduced. These calibration data were provided by the manufacturer in increments of 1 nm for each band. In the software, the transformation of raw pixel values into reflectance basically follows a two-step approach (MicaSense Inc, 2019). First, the raw pixel values of all images were converted to absolute spectral radiance using a camera-specific radiometric calibration model. Here, sensor-specific characteristics like sensor black level and lens vignette effects were compensated. Second, a factor was estimated, allowing for a transformation from radiance to reflectance. At this point, the reflectance values from the CRP calibration data and the radiance values of the CRP images captured in the field were taken into account. Overall, the CRP-based calibration procedure assumes constant lighting conditions over the flight duration. In case CRP images were taken before and after the flight, the reflectance of MS imagery is calibrated based on linear interpolation of the CRP information. In situations with changing conditions in the middle of a flight, the DLS can help to improve reflectance calibration by applying additional corrections image-wise. Although the integration of DLS data was suitable in area#1 and area#2, the approach reached its limits in area#3. Rapidly changing cloud coverage throughout the entire flight impeded an accurate calibration of reflectance. In the event of clouds shadowing the captured image area but not the DLS, radiometric

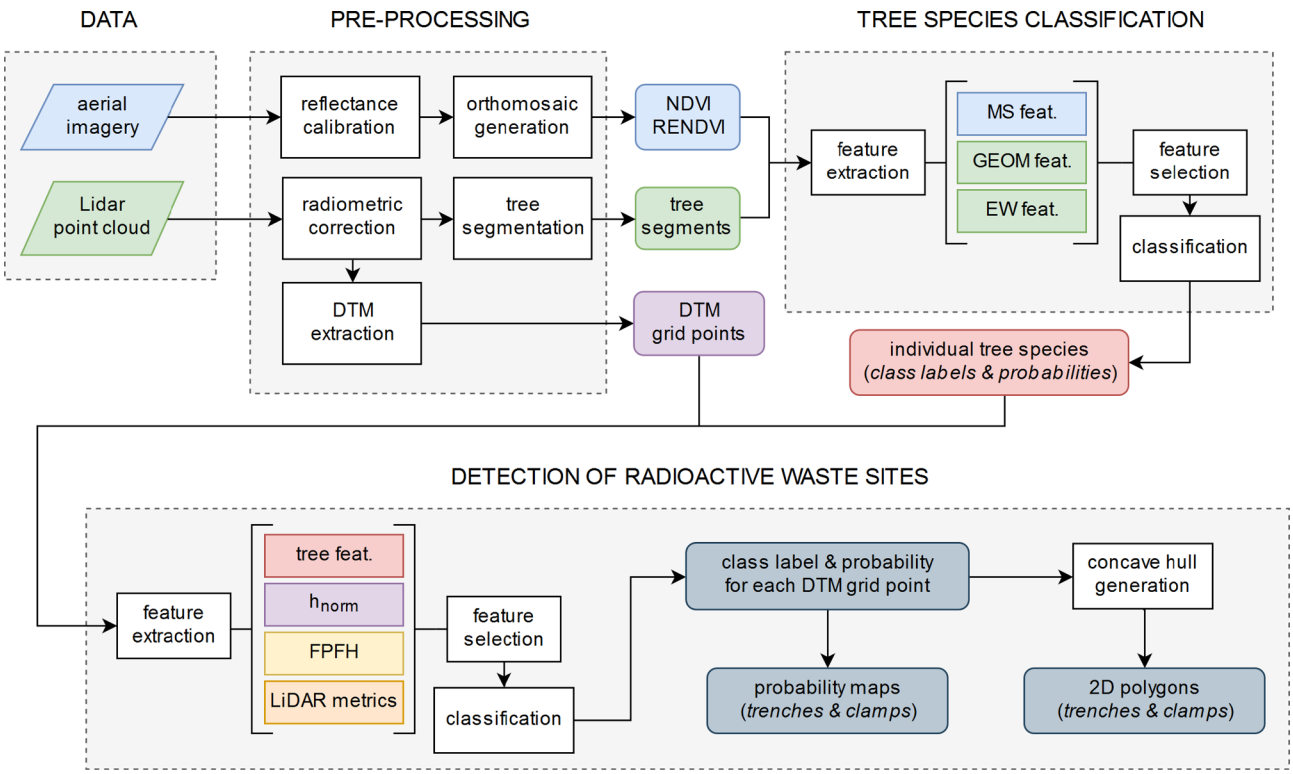

Fig. 5. Overview of the proposed method for detecting radioactive waste sites.

information of the images could not be corrected properly. As a consequence, the MS imagery in area#3 was not used for further investigation. Thus, in this area, tree species classification was only based on the geometric and radiometric features generated from lidar data.

4.2.2. Orthomosaic generation

Based on missing ground control points in overflown inaccessible areas, we registered the photogrammetric data to the georeferenced lidar data. Therefore, different steps in several software packages had to be executed for area#1 and area#2. Initially, the georeferenced lidar point cloud was transformed to the aforementioned photogrammetric dense point cloud via iterative closest point (ICP) algorithm in CloudCompare 2.8 (CloudCompare Development Team, 2019). Here, the root mean squared error was 0.237 m. Then, we utilized Quick Terrain Modeler (Applied Imagery, 2018) to calculate a digital elevation model (DEM) from the transformed lidar point cloud. Next, the resulting 15 cm DEM was exported as a TIFF image and loaded into Agisoft PhotoScan Professional 1.4.1. Here, an orthomosaic with a 10 cm resolution was computed. In this orthorectification procedure, we relied on the precise lidar DEM instead of using a less accurate DEM calculated from a dense photogrammetric point cloud. Subsequently, vegetation index images were calculated. In addition to the widely used NDVI images, RENDVI images (Sims and Gamon, 2002) were created by utilizing the red edge (RE) and near infra-red channels (NIR). The RENDVI (Eq. 1) can be computed as

$$RENDVI = \frac{RE - NIR}{RE + NIR}. \quad (1)$$

Afterwards, the photogrammetric products must be georeferenced. The dense point clouds were transformed in CloudCompare 2.8, utilizing the particular inverse transformation matrix of the aforementioned ICP. Finally, based on the 2D components of these matrices, the orthomosaics were shifted in QGIS 2.18 (QGIS Development Team, 2017).

4.2.3. Radiometric correction of lidar data

In addition to the 3D coordinates of each laser point, the YellowScan Mapper I provides intensity values. The instrument is equipped with an Ibeo LUX 2010® laser unit for generating Gaussian-shaped pulses. According to the technical description, the recorded intensity values are equivalent to the widths Ew_i of the echo pulses measured at a fixed internal threshold g_0 (Fig. 6). In a series of n Gaussian return pulses

$$g(t) = \Sigma_{i=1}^{n} A_i exp\left(-\frac{(t - t_i)^2}{\sigma_i^2}\right), \quad (2)$$

the parameter Ew_i theoretically depends on the shape of the return pulses, which is defined by the pulse width σ_i and amplitude A_i (Eq. 2). Both of these parameters are influenced by the scan angle. Assuming a flat terrain and the Lampertian law for scattering targets, the pulse width σ_i is slightly broadened towards the swath edge of a laser strip.

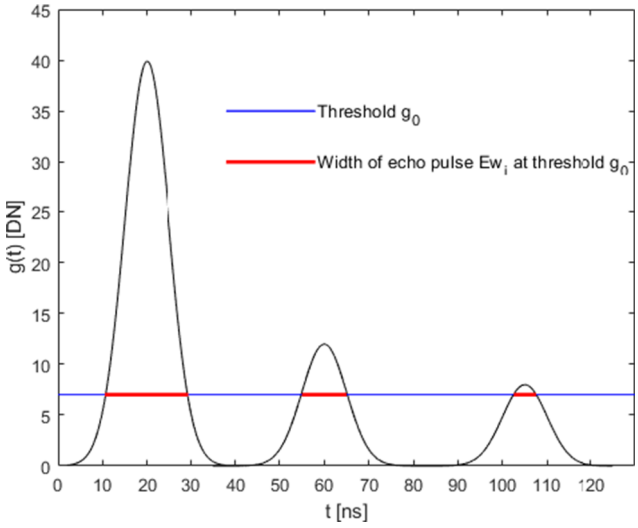

Fig. 6. Definition of parameter *Ew* in YellowScan Mapper I (according to Ibeo Automotive Systems GmbH (2010)).

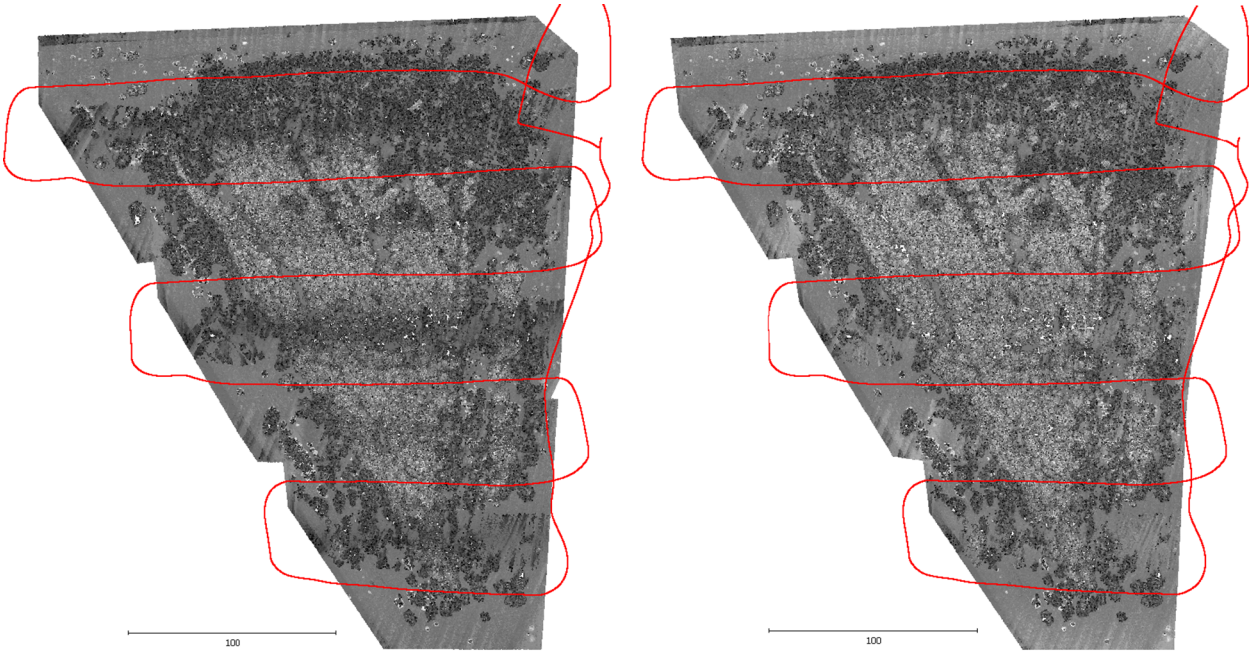

Fig. 7. Ew_i values in area#1, before (a) and after (b) correction; flight lines overlay (red). (For interpretation of the references to color in this figure legend, the reader is referred to the web version of this article.)

Additionally, echo width widening leads to a reduction in the amplitude A_i with respect to the scan angle, assuming that the emitted laser power is constant (Ussyshkin et al., 2009). Furthermore, the amplitude A_i itself is dependent on the square of the distance between the sensor and target, meaning it also depends on the scan angle. In summary, we can theoretically expect a significant change in the shape of the return pulse and, the parameter Ew_i toward the swath edge. To the best of our knowledge, changes in the parameter Ew_i toward the swath edge have not been studied experimentally to date. However, many researchers have evaluated the dependency of intensity ($= A_i \cdot \sigma_i$) and pulse width on the scan angle. Jutzi and Gross (2009) demonstrated that lidar intensity decreases according to the cosine of the scan angle. In principle, the experiments conducted by Kaasalainen et al. (2011) using terrestrial laser scanners confirm this finding. Reitberger et al. (2007) investigated pulse width in forest areas and calculated scan-angle-dependent increases in pulse width of 15%/20° for laser points with well-defined and smooth reflecting areas (i.e., stem points). Additionally, the same study confirmed a decrease in intensity of 13%/20° corrected by the square of the laser distance for ground points.

Fig. 7a illustrates the raw Ew_i values for area#1, where dark areas are a result of the scan angle effect of the raw parameter Ew_i, which was not compensated in the individual laser strips. For 3D vegetation mapping, raw Ew_i values must be corrected to avoid misclassification effects. Our data-driven method corrects the parameter Ew_i based on the incidence angle, which is approximately equal to the sum of the scan angle and roll angle. First, we filter single return points from the ground points in one reference strip and assume that the forest floor has consistent spectral reflectance properties. Second, the raw values of Ew_i for the reference strip are divided into bins of size 1° with respect to the corresponding incidence angle. Third, the mean value and standard deviation (std) of Ew_i are calculated for each bin. Subsequently, a parabola ($R^2 = 0.95$) is fitted to the mean values of Ew_i (see Fig. 8a). The vertex value of the parabola Ew_{ref} and $std(Ew_{ref})$ of the corresponding bin are used as constant parameters in the empirical correction function. The corrected values Ew^i_{corr} are computed as

$$Ew^i_{corr} = (Ew^i_{raw} - Ew^i_{fit}) * \frac{std(Ew_{ref})}{std(Ew^i_{bin})} + Ew_{ref}, \quad (3)$$

where Ew^i_{raw} is the raw value of a single point, Ew^i_{fit} is the reference value of a single point on the parabola, and $std(Ew^i_{bin})$ is the std of the corresponding bin (Eq. 3). Note that the correction function is only valid for one specific flight height because we did not perform drone flights at different altitudes. Fig. 8b presents the result of correction for the reference strip in area#1. The fitted red horizontal line indicates that the mean values of Ew^i_{corr} are independent of the incidence angle. Fig. 7b presents all points in area#1 colored according to their corrected values. Apparently, the edge effects disappear and the parameters Ew^i_{corr} can be used as additional features for 3D vegetation mapping.

4.2.4. Tree segmentation

As a basis for the tree species classification performed at a later stage, single trees were segmented from the lidar point cloud utilizing the TreeFinder software package (PRIMAVISION Technologies GbR, 2017). The implementation is based on the normalized cut algorithm (Shi and Malik, 2000) which is a top-down method for segmenting objects over a discrete graph structure $G = (V, E)$. The vertices V represent individual objects and the edges E correspond to neighborhood topology. The input 3D lidar point cloud is split into disjointed segments to minimize the normalized cut criterion. A recursive bisection of the graph's vertices V into disjointed segments A and B maximizes the intra-segment similarity of objects and minimizes their inter-segment dissimilarity. The normalized cut criterion to be minimized is defined as

$$NCut(A, B) = \frac{Cut(A, B)}{Assoc(A, V)} + \frac{Cut(A, B)}{Assoc(B, V)}, \quad (4)$$

where $Cut(A, B) = \sum_{i \in A, j \in B} w_{ij}$ is defined as the sum of all weights between A and B segments and $Assoc(A, V) = \sum_{i \in A, j \in V} w_{ij}$ is the sum of the weights of all edges ending in A segments (Eq. 4). Following the recommendations of Reitberger et al. (2009), we set the static stopping criterion of the normalized cut segmentation to 0.16. Visual inspection helped to verify that no oversegmentation or undersegmentation occurred. The result of tree segmentation is a set of polygons describing the hulls of single trees, as well as characteristic parameters, such as tree height, crown base height (CBH), and crown volume.

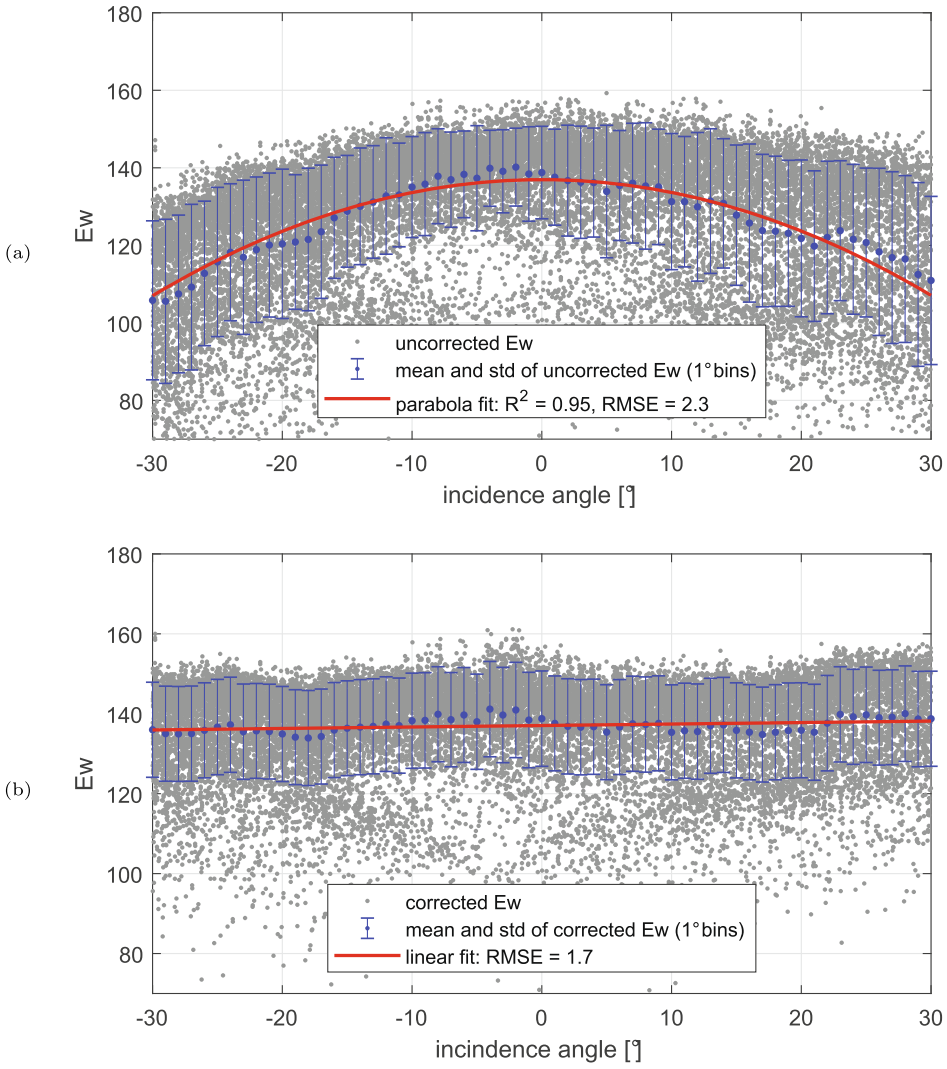

Fig. 8. *Ew* values in the reference strip (area#1).

4.2.5. DTM generation

In the next step, we used the ground routine based on Axelsson (2000) in the commercial software TerraSolid TerraScan™(Soininen, 2016) to filter ground points from the ALS point cloud. The resulting ground points with a point density of approximately five points per m^2 were subsequently interpolated into a 50 cm DTM grid (Polewski et al., 2015). The impact of the DTM smoothing coefficient α on detection results is discussed in Section 5.2.

4.3. Tree species classification

A classic ML approach using the RF classifier requires a set of so-called handcrafted features. These features are typically calculated from the available datasets, adapting as much as possible to the various tasks being addressed. In general, they are engineered manually and are mainly based on statistical terms. For tree species classification, we generated salient features for each tree segment. In total, the feature set consisted of 65 features (Table 6) derived from both lidar and MS data: 32 geometry features (*GEOM*), 14 *Ew*-based features (*EW*), and 19 MS features (*MS*), including statistics calculated from the NDVI and RE-NDVI. Thereafter, the feature space was reduced and an RF classifier was trained to classify tree segments as species of birch, pine, and alder. Note that the detailed classification strategy will be presented in Section 4.5.

Table 6
Feature set for tree species classification; *GEOM#(1–20)* are adopted from Næsset (2004), *GEOM#(21–32)* and *EW#(1–14)* from Reitberger (2010).

Features	Definition	Quantity
GEOM#(1–10)	Density distribution of points per height layer	10[1]
GEOM#(11–20)	Vertical distribution of the tree substance per height layer	10
GEOM#(21–30)	Mean distance of points to the segment center	10
GEOM#(31–32)	Standard deviation (std) of the distance of crown points to the segment center, in x and y direction	2
EW#1	Mean *Ew* of points of a single tree	1
EW#(2–11)	Mean *Ew* of points of a single tree per height layer	10
EW#12	(Σ middle/ Σ first) reflections	1
EW#13	(Σ single/ Σ first) reflections	1
EW#14	(Σ first + Σ middle)/(Σ single + Σ last) reflections	1
MS#(1–8)	NDVI max/min/max-min/mean/std/quartiles[2]	8
MS#(9–16)	RENDVI max/min/max-min/mean/std/quartiles[2]	8
MS#(17–19)	Entries of covariance matrix of NDVI and RENDVI	3
		Σ 65

[1] Increasing numbering from bottom (1) to top (10).
[2] 1st, 2nd, 3rd.

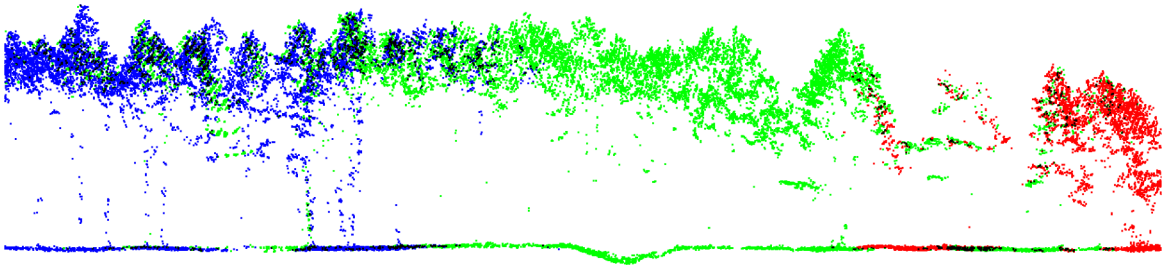

Fig. 9. Cross section of lidar point cloud in area#1 showing possible trench. Points are colored according to flight line. (For interpretation of the references to color in this figure legend, the reader is referred to the web version of this article.)

Table 7
Feature subsets for detection of radioactive waste sites.

Feature subset	Definition	Quantity
TF	Tree-based features	19
h_{norm}	Normalized DTM height	1
FPFH	Fast point feature histograms	33
LM	Lidar metrics	133
		Σ 186

4.4. Detection of radioactive waste sites

The main characteristics of radioactive burials are slight ground settlements (Fig. 9) or elevations and vegetation anomalies in the surrounding areas (see Section 2.2). Therefore, we utilized the results of tree species classification and DTM extraction to prepare a feature set containing handcrafted tree-based features *TF*, normalized DTM height h_{norm}, fast point feature histograms *FPFH* and lidar metrics *LM* (Table 7).

Vegetation anomalies are supposed to be an indicator for the existence of radioactive burials. Therefore, we calculated 19 *TF* based upon the results of prior 3D vegetation mapping (Table 8). In general, the resolution of all generated *TF* was 5x5 m. For each grid point, nearby trees were found by applying a range search within a radius r_{tree} describing a local neighborhood. Then, the feature set was derived based on the information of these filtered tree segments. Initially, the number of neighboring trees resulted in *TF#1*. Next, the tree attributes tree height, CBH, and crown volume were used to generate features *TF#(2–7)* that represent the mean and std of these three attributes within the circular neighborhood. *TF#(14–15)* were based on the area size of the tree polygons. For each filtered tree, the crown diameter D_{cr} was calculated from the crown size by assuming a circular crown shape, resulting in *TF#(16–17)*. Moreover, ratios describing the frequencies of individual tree species in each neighborhood were defined as *TF#(8–10)*. Additionally, for each tree class, tree species classification also provided the class probabilities p_i for each tree segment. The mean p_i values of neighboring trees were used to define the features *TF#(11–13)*. Finally, we estimated the total above-ground biomass P_a of individual trees. To this end, we utilized a transcontinental allometric model developed for the main Eurasian tree species using tree height H and crown diameter D_{cr} as regressors. We estimated P_a using the allometric function

$$lnP_a = a_0 + a_1 lnH + a_2 lnD_{cr} \quad (5)$$

to generate features *TF#(18–19)*. Eq. 5 and the coefficients a_0, a_1, and a_2 for the tree species of pine, birch, and alder were taken from Usoltsev et al. (2019).

Prior experiments have demonstrated that the normalized DTM height h_{norm} is a promising feature for describing terrain height anomalies (Briechle et al., 2018). This feature was calculated by reducing the corresponding absolute terrain height h_{DTM} for each DTM grid position by h_{trend} (Eq. 6):

$$h_{norm} = h_{DTM} - h_{trend} \quad (6)$$

h_{trend} is the mean height in a surrounding quadratic area defined by an edge length e_{trend} and is calculated for every DTM grid point using a sliding window approach.

Because the shape of trenches and clamps is cylindrical, local shape descriptors are a promising feature set because they are able to distinguish between different geometric shapes (plane, cylinder, sphere, etc.). We calculated a set of FPFH (Rusu et al., 2009), an enhanced version of point feature histograms (Rusu et al., 2008), which were developed for real-time robotics applications. Retaining most of the power of the point feature histograms, these features are invariant to 3D translations or rotations and robust to varying point density and noisy datasets. As input data, we utilized filtered ground points from the lidar data, with a point density of approximately five points per m^2 in forested areas. Initially, normal vectors were computed for each ground point. Here, the neighborhood size was defined by a radius r_N. Next, FPFH features were calculated for each point of a synthetic 2 × 2 m grid. In detail, geometric properties were estimated by modeling the relationships between surface normals to characterize the local geometry in the area around each grid point. This calculation is based on the analysis of the eigenvectors and eigenvalues of the covariance matrix formed by points within a circular neighborhood defined by a radius r_{FPFH}. Based on the angular differences between each pair of normals, a normalized multidimensional histogram was computed, leading to a total of 33 FPFH features.

The feature set was completed with 133 height- and density-dependent lidar features to characterize vegetation. Based on the raw 3D point cloud, these lidar metrics (Næsset, 2004) were computed for quadratic cells defined by a cell size e_{cell}. In detail, features were

Table 8
Definition of tree-based features *TF*.

TF#	Feature	Definition
1	*tree_amount*	Number of trees
2	*tree_height_mean*	Mean tree height [m]
3	*tree_height_std*	Std of tree height [m]
4	*CBH_mean*	Mean CBH[1] [m]
5	*CBH_std*	Std of CBH [m]
6	*crownVol_mean*	Mean crown volume [m^3]
7	*crownVol_std*	Std of crown volume [m^3]
8	*treeClass0_ratio*	Pine tree ratio (Σ pines/ Σ trees)
9	*treeClass1_ratio*	Alder tree ratio (Σ alders/ Σ trees)
10	*treeClass2_ratio*	Birch tree ratio (Σ birches/ Σ trees)
11	*pred0_mean*	Mean pine probability
12	*pred1_mean*	Mean alder probability
13	*pred2_mean*	Mean birch probability
14	*areaSize_mean*	Mean 2D tree dimension [m^2]
15	*areaSize_std*	Std of 2D tree dimension [m^2]
16	D_{cr}_mean	Mean crown diameter [m]
17	D_{cr}_std	Std of crown diameter [m]
18	*biomass_mean*	Mean above-ground biomass [kg]
19	*biomass_std*	Std of above-ground biomass [kg]

[1] crown base height.

generated for 10 different height layers (0–1.5 m, 0.5–2 m, 0.5–5 m, 1.5–5 m, 5–12 m, > −0.5 m, < 0 m, > 0 m, > 2 m, > 12 m). Note that the decisive control parameters for extracting the overall feature set were optimized in a sensitivity analysis (see Section 5.2), leading to a final list of best-performing parameters. Moreover, the complete feature set consisting of 186 individual features was bilinearly resampled to a grid of 50 cm resolution which is congruent to the DTM. We used this feature set to train an RF classifier (see Section 4.5) for categorizing DTM grid points into the classes "trench", "clamp" or "non-contaminated". Next, polygonal objects were generated from DTM grid points which showed a trench or clamp probability of more than 95% as concave hulls. Finally, isolated classification errors were eliminated using an area threshold of 30 m^2.

4.5. Classification strategy

In our study, we utilized RF classifiers for the classification of both tree species and radioactive waste sites. This popular supervised ML method has proven to achieve high-quality results in typical remote sensing tasks like land cover classification (Pal, 2005; Rodriguez-Galiano et al., 2012) and tree species classification (Immitzer et al., 2012; Puissant et al., 2014). By now, this type of classifier has been implemented in various programming languages. In our experiments, we used the randomForest package (Liaw and Wiener, 2002) in R (R Core Team, 2018). In the preprocessing procedure, the high-dimensional feature space was gradually reduced to avoid overfitting. At the beginning, highly correlated redundant features were deleted from the feature set to avoid deterioration of classification accuracy. This process was based on the application of a threshold to feature-to-feature cross-correlation. First, a covariance matrix was calculated. Second, a cross-correlation threshold θ was used to eliminate high pair-wise redundancy. Specifically, one feature of any feature pair with a correlation coefficient exceeding θ was eliminated. Different θ values (0.85, 0.90, 0.95, 1.00) were tested to find an optimal threshold. To investigate the capability of the proposed handcrafted feature subsets, RF classifiers were trained on these reduced datasets. Next, an RF model was built using all feature subsets. Three iterations of fivefold cross-validation were used to derive average OA and κ values. The number of trees was set to 500, with a minimum size for the terminal nodes of one. Generally, trees were grown to the maximum depth. The parameter controlling size of the samples to be drawn per node was equal to the number of training samples. Furthermore, the number of features randomly sampled as candidates at each split was set to the square root of the number of total features. Finally, the optimal model was selected based on the metric "accuracy". In general, irrelevant features can have a negative impact on model accuracy. Therefore, it is essential to perform feature selection prior to building the final model. On a smaller and more robust dataset, both overfitting and training time can be reduced. In the literature, a backward feature selection technique based on the recursive feature elimination (RFE) algorithm has been recommended quite often (Ma et al., 2017; Gregorutti et al., 2017). At the beginning, this algorithm trains an RF model on the overall feature set. Thereby, the relevance of individual features can be computed based on the mean decrease in accuracy. Then, the least important features can be recursively excluded from the feature space until a final best performing set is obtained. In the present study, we utilized the RFE algorithm from the caret package (Kuhn, 2008) in R and set the "rerank" parameter to "false". Thus, the variable importance was not recalculated each time features had to be removed. Based on the corresponding OA value, the resulting RFE model was compared to the RF model containing all available features. Finally, the RFE model was utilized to calculate class predictions $pred_i$ and class probabilities $prob_i$ for each sample. In all study areas, the quality of the final RFE model was verified by comparing the predicted labels and real values of the particular test dataset. For quantitative evaluation, a confusion matrix was generated and quality metrics (OA, κ, precision, recall, F1) were derived. Furthermore, we investigated the transferability of the trained classifiers. Therefore, the classifier optimized on study area#1 was applied to all labeled data of area#2.

Table 9
Results of tree species classification.

	Area#1	Area#2	Area#3
Training samples	180	162	204
GEOM	83.4 (0.750)[1]	81.7 (0.725)	76.7 (0.650)
EW	85.9 (0.787)	75.6 (0.633)	78.7 (0.681)
MS	87.2 (0.812)	86.1 (0.792)	—[2]
All subsets (RF)	87.6 (0.814)	88.5 (0.828)	80.9 (0.713)
All subsets (RFE)	**90.2** (0.853)	**90.0** (0.850)	**81.3** (0.720)
Gain in OA	2.6	1.5	0.4
Feat. reduction	35.8%	46.3%	41.3%
Top 7 feat.	*EW#1*	*MS#7*	*EW#1*
	MS#8	*EW#1*	*EW#11*
	EW#10	*EW#11*	*EW#10*
	EW#11	*EW#10*	*GEOM#11*
	GEOM#9	*GEOM#9*	*EW#13*
	GEOM#31	*MS#15*	*EW#14*
	MS#15	*GEOM#31*	*GEOM#9*
Test samples	45	42	51
All subsets (RFE)	**88.9** (0.832)	**88.1** (0.821)	**78.4** (0.677)
pine	0.88 / 0.94 / 0.91[3]	0.92 / 0.86 / 0.89	0.89 / 0.89 / 0.89
birch	0.88 / 0.82 / 0.85	0.80 / 0.86 / 0.83	0.72 / 0.76 / 0.74
alder	0.92 / 0.92 / 0.92	0.93 / 0.93 / 0.93	0.73 / 0.69 / 0.71

[1]OA in %, κ in brackets.
[2]For area#3, no accurate MS data were available.
[3]precision/ recall/ F1 score.

5. Experiments

5.1. Tree species classification

RF classifiers (θ = 0.90) using all feature subsets achieved an OA of 90.2% (κ = 0.853) in area#1, 90.0% (κ = 0.850) in area#2, and 81.3% (κ = 0.720) in area#3 (Table 9). Using only individual feature subsets, the average OA values were 80.6% (geometry features), 80.1% (*Ew*-based features), and 86.7% (MS features). Here, κ ranged from 0.633 to 0.812. Depending on the study area, backward feature selection (RFE) improved the OA by 0.4% (area#3) to 2.6% (area#1, see Fig. 10). Furthermore, the dimensions of feature spaces were significantly reduced (average reduction of 41.1%). On the test datasets,

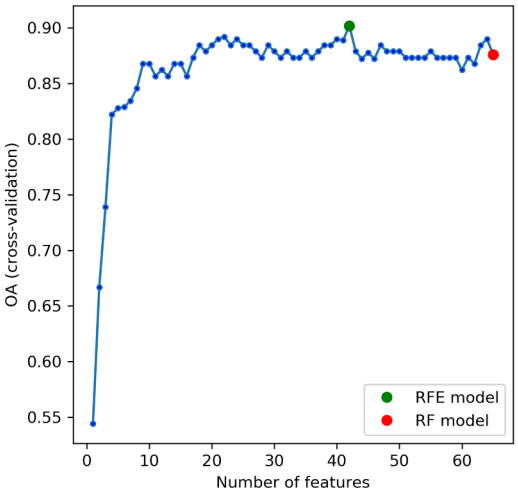

Fig. 10. RFE result for tree species classification in area#1.

Table 10
Control parameters.

Parameter	Definition	Tested values	Optimized value
r_{tree}	Radius to identify close-up trees	3 m, 5 m, 10 m, 20 m, 30 m	5 m
α	DTM smoothing coefficient	1 to 10 (step size of 1)	3
e_{trend}	Edge length of quadratic area to calculate DTM trend	0.5 to 45.5 m (step size of 5 m)	5.5 m
r_n	Radius used to compute surface normals	1.5 to 5.0 m	3.0 m
r_{FPFH}	Radius used to generate FPFH	2.0 to 10.0 m	7.0 m
e_{cell}	Cell size for calculation of lidar metrics	2 × 2 m, 5 × 5 m, 10 × 10 m	5 × 5 m

the trained classifiers achieved OA values of 88.9% (area#1), 88.1% (area#2), and 78.4% (area#3). Here, the mean F1 scores were 0.90 (pine), 0.81 (birch), and 0.85 (alder).

The seven best features for each study area were ranked according to the mean decrease in accuracy. Features from all three feature subsets were ranked among the seven most important features. The most relevant feature was the mean *Ew* value of all laser points for a single tree (*EW#1*). Other important *Ew*-based features were the mean *Ew* value of points in the two top height layers of trees (*EW#10*, *EW#11*), as well as the features describing penetration (*EW#13*, *EW#14*). Geometry features ranked in the top seven were related to crown density (*GEOM#9*), crown shape (*GEOM#31*), or the occurrence of points in the lowest height layer of trees (*GEOM#11*). The most important MS features were the second and third quartile of the NDVI values (*MS#7*, *MS#8*), as well as the second quartile of the RENDVI values (*MS#15*) inside a tree polygon.

5.2. Sensitivity analysis

The four feature subsets used for the detection of trenches and clamps are dependent on six decisive control parameters (Table 10) that must be optimized through sensitivity analysis. During this optimization process, we used the OA value of the RF classifier as a quality measure. Different radii r_{tree} for neighborhood definition for the selection of nearby trees were tested. The value of 5 m yielded the best performance. Therefore, the circular area size for the creation of *TF* was 78.5 m^2. The key parameter for the generation of h_{DTM} is the DTM smoothing coefficient α (Polewski et al., 2015). Values ranging from 1 to 10 were evaluated and the optimal α value was determined to be three. For the computation of h_{trend}, the decisive parameter is the size of the surrounding quadratic area. Areas with a varying side length e_{trend} were tested and the best OA was achieved with e_{trend} = 5.5 m. The radii r_N and r_{FPFH} defining the neighborhood for the computation of surface normals and FPFH generation were also optimized. Fourteen combinations of parameters were tested. The optimal values were r_N = 3.0 m and r_{FPFH} = 7.0 m. Finally, the cell size e_{cell} for the calculation of lidar metrics was set to 5 × 5 m.

5.3. Detection of radioactive waste sites

5.3.1. Classification results

For the detection of trenches and clamps, the mean OA of the RF classifiers (θ = 0.90) was 98.9% for the training data and 98.2% for the test data (Table 11). In general, the recall and precision for the class "non-contaminated" were 0.97 or higher in all study areas, leading to excellent F1 scores. Furthermore, the recall values for "trench" were at least equal to 0.98, whereas the precision values ranged between 0.37 and 0.62. Apparently, numerous DTM pixels were predicted as trench pixels although labeled as "non-contaminated". Moreover, in area#3, the RF classifier reached an F1 score of 0.80 for the class "clamp" (precision = 0.66, recall = 1.00).

A reduction of the feature sets to individual feature subsets led to mean OA values of 88.7% (*TF*), 71.6% (h_{norm}), 93.9% (*FPFH*), and 95.3% (*LM*). By including the RFE step, the feature space was considerably reduced by an average of 40.2% and the gain in OA was 0.23%. Feature relevance assessment clearly demonstrated that members of all four feature subsets are represented in the final list of the 10 most important features. The normalized DTM height h_{norm} is ranked here, as well as the features *FPFH#(16–18,27,28)*. The most important lidar metrics are features that describe the terrain surface and vegetation below 1.5 m, namely the mean value of points with a negative height *LM_mean(h < 0 m)* or a height below 1.5 m *LM_mean (h < 1.5 m)* and the minimum height of all points *LM_min(h)*. *TF* utilizing tree height (*TF#(2,3)*), mean CBH (*TF#4*), and mean crown diameter (*TF#16*) are also contained in this ranking. Furthermore, species-related features, namely alder tree ratio (*TF#9*) and mean alder probability (*TF#12*), seem to be of importance for the waste site classification. The *TF* comprise approximately 27% of the top 10 features among all areas (eight out of 30). Besides the estimated class labels, we also calculated the class probabilities for each DTM pixel. From these values, probability maps (Fig. 11b) were created showing DTM grid points classified with more than 95% as "trench". The results are highly correlated to the DTM height (Fig. 11a). In the last step, polygonal objects were generated from classified DTM pixels as concave hulls. To clean up the results, we set an area threshold of 30 m^2 to remove small objects that were obviously generated by clusters of wrongly classified DTM pixels. Finally, an overview of all the detected radioactive burials was created (Fig. 15).

We now focus more on the spatial distribution of the classification errors. Fig. 12a shows the normalized DTM height and the manually produced polygons that were used to label the DTM pixels in area#1. Fig. 12b illustrates the classification errors on the test dataset (OA = 99.1%, κ = 0.758) and highlights the errors. On the one hand, false positives (FP) appear in the transition zone from trench to non-contaminated areas. On the other hand, some accumulated FP occur, and these are not correlated to the normalized DTM height in most cases. The results in area#2 (OA = 98.2%, κ = 0.744) are mostly comparable to those of area#1. In area#3 (OA = 97.2%, κ = 0.609), a large number of non-contaminated pixels were wrongly classified as trench pixels (22,491). A closer look at these grouped FP demonstrates that they strongly resemble the typical shape of trenches (Fig. 13a). Moreover, they are correlated to the normalized DTM height. Furthermore, we could find a fairly high number of FP (4613) for the class "clamp". However, most of these errors are only located in the transition zone from clamp to non-contaminated areas (Fig. 13b).

5.3.2. Classifier generalization

In addition to classifier evaluation on manually labeled test data in the same study area, we conducted an experiment to investigate the generalization capabilities of the trained classifiers. The classifier trained for area#1 was applied to the entire dataset of area#2. If we analyze the relevant confusion matrix (Table 12), we can notice a considerable high number of FN (6440) and FP (9719) causing a relatively low F1 score for the class "trench" (0.49). Note that the extremely high number of TN (227,752) still led to an excellent OA (93.6%). For a section of area#2, Fig. 14b shows the spatial distribution of the classification errors. Apparently, in some areas, numerous FP were generated in the vicinity of DTM pits (Fig. 14a).

Table 11
Classification results for detection of radioactive waste sites.

	Area#1	Area#2	Area#3
Training samples	6222	14,310	22,872
TF	88.5 (0.841)[1]	90.7 (0.893)	86.9 (0.851)
h_{norm}	79.7 (0.590)	71.1 (0.422)	64.0 (0.460)
FPFH	96.1 (0.914)	95.4 (0.917)	90.1 (0.852)
LM	95.3 (0.910)	95.9 (0.926)	94.6 (0.923)
All subsets (RF)	98.9 (0.972)	99.4 (0.987)	97.6 (0.961)
All subsets (RFE)	**99.1** (0.982)	**99.6** (0.992)	**97.9** (0.968)
Gain in OA	0.2	0.2	0.3
Feat. reduction	43.4%	64.1%	13.2%
Top 10 feat.	*FPFH#16*	*LM_mean(h < 0 m)*	*FPFH#16*
	FPFH#18	*FPFH#16*	*LM_mean (h < 0 m)*
	LM_mean (h < 0 m)	*TF#3*	*LM_min(h)*
	TF#4	*FPFH#18*	*FPFH#18*
	LM_min(h)	*TF#2*	h_{norm}
	h_{norm}	*LM_mean (h < 1.5 m)*	*LM_mean (h < 1.5 m)*
	TF#12	h_{norm}	*TF#4*
	FPFH#27	*TF#12*	*FPFH#28*
	FPFH#17	*FPFH#28*	*FPFH#27*
	TF#16	*FPFH#27*	*TF#9*
Test samples	208,704	251,561	1,015,037
All subsets (RFE)	**99.1** (0.758)	**98.2** (0.744)	**97.3** (0.609)
non-contaminated	1.00 / 0.99 / 1.00[2]	1.00 / 0.98 / 0.99	1.00 / 0.97 / 0.99
trench	0.62 / 0.99 / 0.76	0.61 / 0.98 / 0.75	0.37 / 0.98 / 0.54
clamp	—	—	0.66 / 1.00 / 0.80

[1]OA in %, κ in brackets.
[2]precision/ recall/ F1 score.

5.3.3. Classifier evaluation using ground truths

First, the classifier trained on area#3 was applied to geometrically incorrect and incomplete RWTSP reference data from area#3. Here, the classification accuracy was relatively low (Table 13). Specifically, 55.7% (39,328 out of 70,598) of the DTM grid points located in the RWTSP trench areas were classified as "non-contaminated". Note that the quality of these reference data is poor because these data are based on nonprofessional generation techniques (see Section 3.2). Second, 38 borings (Fig. 15) verified the existence (25) or absence (9) of buried radioactive biomass and demolition waste in 34 cases (OA = 89.5%). In four cases (borings C132, C151, C155 and C221), radioactive waste was found in areas that had been classified as "non-contaminated". However, these FN are located only 3–9 meters off the detected trenches. All deposits occurred at an average depth of 1–2 m, exhibiting EDR values that were up to 30 times greater than those on the terrain surface (Tables 1 and 2).

6. Discussion

6.1. Tree species classification

6.1.1. Classification results

In general, the results demonstrate that the three main tree species in the ChEZ (birch, alder, and pine) were successfully classified using both lidar data and MS imagery. Moreover, the low decrease in classification results on the test data compared with training data (1.3–2.9 percentage points) indicates a fairly good generalization quality. The best results were achieved in the case of the available MS data in area#1 and area#2 (mean OA = 88.5%, mean κ = 0.827). These results are highly comparable to Kaminska et al. (2018), who classified six classes of trees with an OA of 88.6% (κ = 0.851) fusing color-infrared (CIR) imagery and leaf-off ALS data with normalized intensity values. Without MS data (area#3), the OA decreased to 78.4% (κ = 0.677). In our experiments, MS features generated from five spectral channels clearly increased the classification result by approximately 10%. This finding corresponds to Holmgren et al. (2008) and Ørka et al. (2012), who also demonstrated a significant improvement in classification results by including information from MS images. Regarding the single tree species, the overall F1 score for pine (0.90) was generally better than for the deciduous species birch (0.81) and alder (0.85). Even

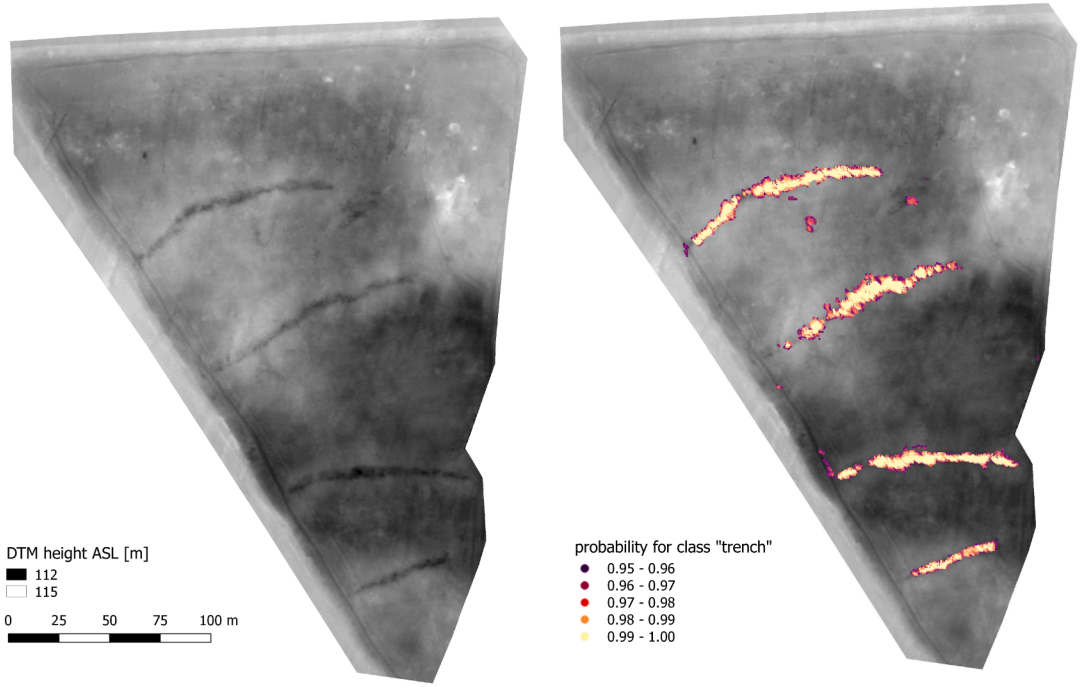

(a) DTM raster (cell size = 50 cm).

(b) Probability map showing DTM pixels classified as "trench".

Fig. 11. Classification result for area#1.

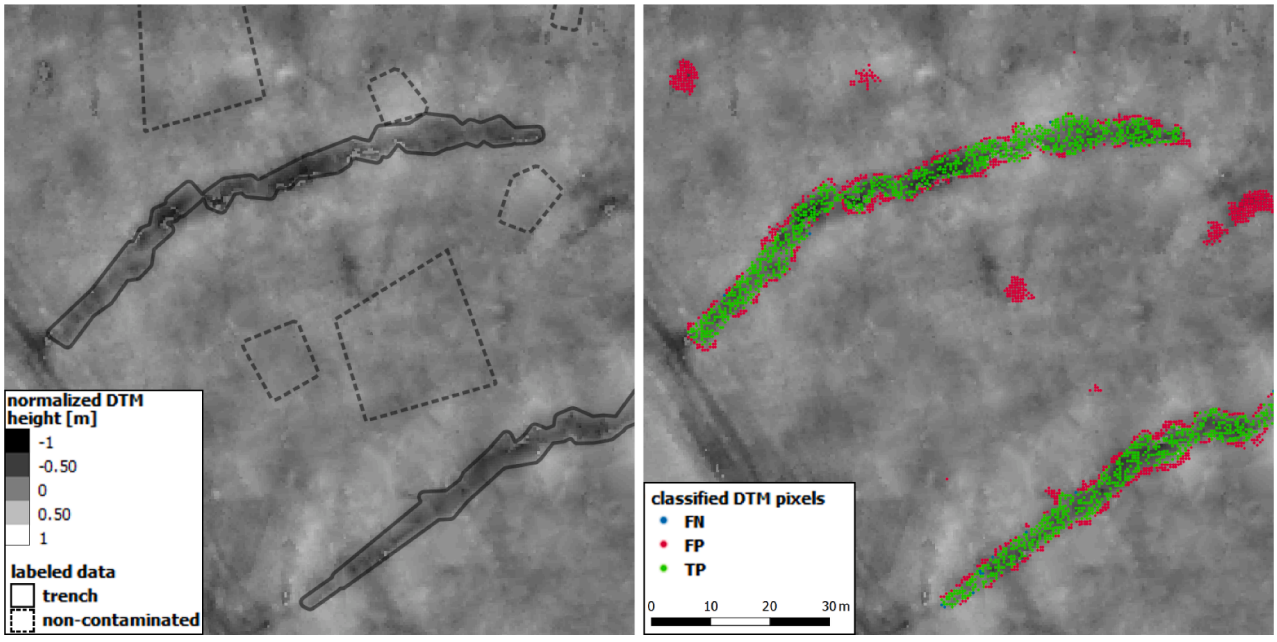

(a) Normalized DTM height and manually produced class boundaries used to label the dataset.

(b) Classification errors on test data (OA = 99.1%, κ = 0.758); TP = true positives, FP = false positives, FN = false negatives; Non-coloured pixels outside the trench areas are true negatives (TN), whereas non-coloured pixels inside the trench areas were used for training and are therefore not shown as test results.

Fig. 12. Classification errors for detection of trenches (section of area#1).

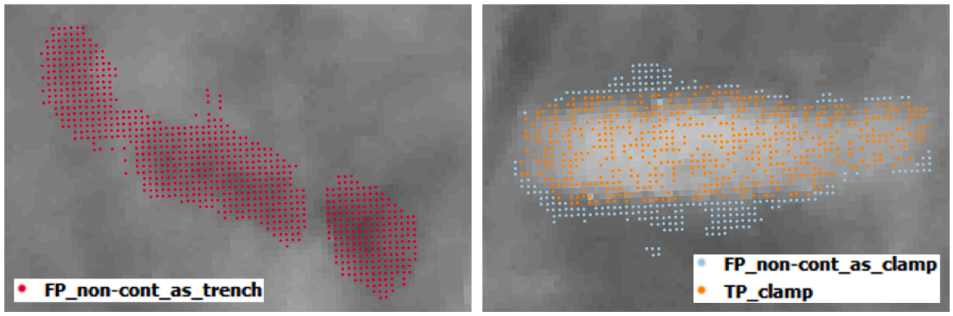

(a) FP for class “trench”.

(b) FP for class “clamp”.

Fig. 13. Classification errors (section of area#3).

without MS features (area#3), pines were classified with a F1 score of 0.89. Obviously, MS features primarily improved the classification of birch and alder. This is because at the time of data collection, birches had already sprouted. Therefore, their characteristic spectral appearance supported the classification significantly.

6.1.2. Feature importance

Furthermore, feature selection led to a significant reduction of the feature space and improved the OA by 1.5% on average. According to the feature relevance assessment, the mean *Ew* value of all laser points for a single tree was the most relevant feature. This fact substantiates the quality of our newly introduced data-driven correction method for radiometric lidar data of the YellowScan Mapper I laserscanner. Moreover, geometry- and *Ew*-based features related to the tree crown and penetration of the laser beam to the ground were also among the top seven features. This is in full accordance with Shi et al. (2018b) and Amiri et al. (2019), showing that these types of features mainly control the quality of tree species classification. In our experiments, certain quartiles of the NDVI and RENDVI values significantly enhanced the classifier. Regarding the feature subsets, the *MS* features provided better results than the lidar-related features (*GEOM*, *EW*). A classifier using only the *MS* features was only slightly worse than the classifier using the complete feature set.

Table 12
Results for applying the classifier trained for area#1 to the dataset for area#2 (OA = 93.6%).

		prediction		evaluation metrics		
		non-cont.[1]	trench	precision	recall	F1
reference	non-cont.	227,752	9,719	0.97	0.96	0.97
	trench	6,440	7,650	0.44	0.54	0.49

[1] non-contaminated

[1] non-contaminated

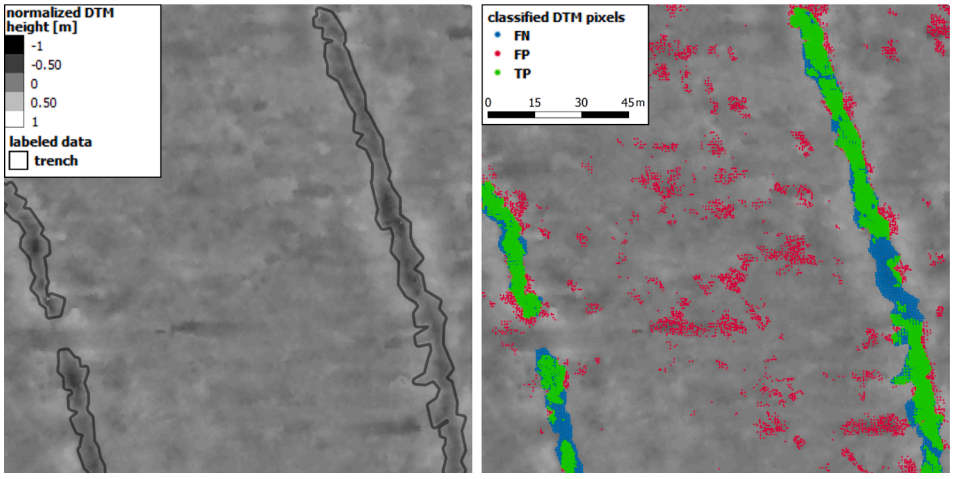

(a) Normalized DTM height and class boundaries used to label the test dataset.

(b) Classification errors of the classifier trained for area#1 applied to a section of area#2.

Fig. 14. Generalization capabilities of the classifier (section of area#2).

Table 13
Results for applying the classifier trained for area#3 to the RWTSP reference data (OA = 65.1%).

		prediction			evaluation metrics		
		non-cont.	trench	clamp	precision	recall	F1
reference	non-cont.	39,749	111	16	0.48	1.00	0.65
	trench	39,328	28,535	2,735	0.95	0.40	0.57
	clamp	3,453	1,391	19,439	0.88	0.80	0.84

6.2. Detection of radioactive waste sites

6.2.1. Classification results

Our results show that the area-wide detection of unknown radioactive burial sites in the forested areas of the ChEZ can be performed successfully using both UAV-based lidar data and MS imagery. A classification accuracy of over 97% for DTM grid points potentially located in areas with buried radioactive materials is relatively high for all study areas. By including a feature selection technique, we removed redundant and irrelevant features from the dataset and effectively

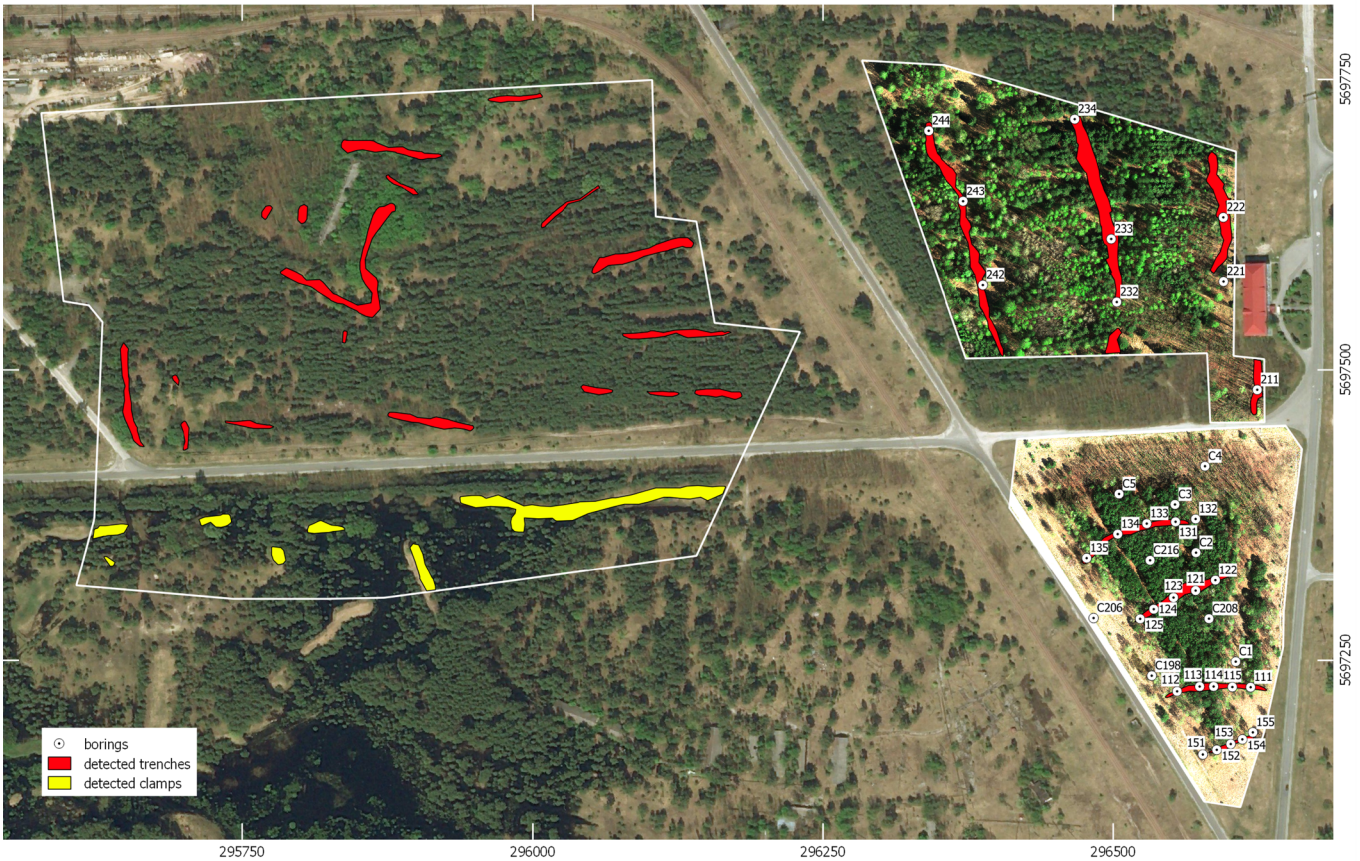

Fig. 15. Detected burial sites (trenches and clamps) and conducted borings in the study areas; Coordinate system: UTM zone 36 N (EPSG 32636); Base map source: bing map ©Microsoft Corporation.

avoided overfitting for a standard RF classifier. The OA values of the proposed classifiers on the test datasets are comparable to the results of a fivefold cross validation that we performed during classifier training. However, FP in the transition zones from burials to non-contaminated areas caused a decrease in the precision values for both trenches and clamps. Manual generation of reference data based on visual DTM interpretation may certainly affect these errors. In area#3, we realized that approximately 30% of the FP are grouped in longish clusters and, thus, strongly resemble the typical shape of trenches. Moreover, they are correlated to the normalized DTM height. Based on the results for the class "trench" in area#1 (F1 = 0.76) and area#2 (F1 = 0.75), we assume that the classification accuracy for trench pixels is actually higher. Because of missing ground reference data in this study area, we can only speculate that these grouped errors are located in trenches that were not considered during manual labeling. Theoretically, if these 30% of rather obvious FP samples were taken into account in area#3, the F1 score for "trench" would improve from 0.54 to approximately 0.72.

6.2.2. Feature importance

A feature relevance assessment supported the classification results and demonstrated that handcrafted features from all the subsets appear among the most important features. Clearly, local shape descriptors are very significant features for modeling the cylindrical shapes of both trenches and clamps. Two FPFH features (*FPFH#16* and *FPFH#18*) were ranked in the top four features for all study areas. Unsurprisingly, the normalized DTM height h_{norm} is a promising feature in all three study areas. Regarding the lidar metrics, we observed that the most important variables are features describing the terrain surface and low structures. In addition to the features describing the terrain geometry, the newly developed *TF* comprise approximately 27% of the top 10 features for all study areas, meaning they also had a significant impact on the classification results. Aside from the features describing the tree geometry (*TF#(2–4,16)*), species-related features such as alder tree ratio (*TF#9*) and mean alder probability (*TF#12*) are capable of further improving the proposed classifier. For example, it appears that alder trees preferably grow in the vicinity of the trenches of area#1 and area#2. In summary, tree species classification is beneficial for detecting radioactive waste sites in the ChEZ.

6.2.3. Transferability between study areas

To a certain degree, the capabilities of the trained classifier for trench detection in area#1 were transferable to adjacent area#2 (OA = 93.6%). Compared with the results of an RF classifier being trained directly in study area#2, the F1 score for non-contaminated DTM pixels remained almost unchanged (F1 = 0.97). Nevertheless, a considerable high number of misclassified DTM pixels caused clearly worse results for the class "trench" (F1 = 0.49). When analyzing the spatial distribution of these errors, we observed that numerous FP were generated in the vicinity of DTM pits. Furthermore, comparing the feature importance of the classifiers trained in area#1 and area#2, it seems that some of the *TF* are disadvantageous for classifier generalization. Namely, the mean CBH is ranked 4th in area#1, whereas the mean and std of the tree height are in the top five features in area#2. Due to different characteristics regarding the tree geometry (crown shape, tree height), these *TF* vary between the study areas. However, these differences could not be detected in a visual interpretation of the dataset. The importance of features related to the terrain geometry is less fluctuating. In other words, these features should be focused on if a generalization of the classifier is to be considered. Unsurprisingly, when using geometrically incorrect and incomplete RWTSP reference data (see Section 3.2.1), the OA is relatively low (OA = 65.1%).

6.2.4. Verification based on ground truths

A comparison of detection results and 38 borings clearly shows that 25 TP and 9 TN could be verified in area#1 and area#2 (OA = 89.5%). Only four FN occurred less than 9 m off the detected trenches, meaning the classifier falsely predicted areas as "non-contaminated". In summary, EDR measurements inside the bore holes confirmed the existence of suspected trenches that were unknown and not identified prior to the application of our methodology. Furthermore, EDR measurements revealed that the radioactive waste in the trenches was covered with a layer of approximately 0.5 m of "clean" sand. This layer shielded the active inventory. Therefore, these radioactive waste burials were not detected by standard EDR measurements.

6.2.5. Comparison to previous studies

To the best of our knowledge, the detection of radioactive burials using remotely sensed optical data has never been performed before. Thus, there is a lack of comparable studies. Nevertheless, our task is partially similar to certain research in the archaeology community. For example, Guyot et al. (2018) detected burial mounds based on the normalized height calculated from a 25 cm DTM. Furthermore, Lasaponara et al. (2010) demonstrated that micro-elevation changes in lidar-based DTMs support the identification of archaeological sites. Interestingly, our method significantly outperforms UAV-based gamma spectrometry surveys (Zabulonov et al., 2015), which have a detection rate of approximately 50% in vegetated areas. Moreover, compared with a historical map created from the memories of so-called liquidation workers (Fig. 2), the quality of our precise and reliable mapping approach is enormous.

6.3. Limitations of method

Despite fairly good results, our methodology has some limitations. Needless to say, the detection of radioactive waste sites greatly depends on the resolution of the lidar-based DTM. As stated by other studies, ground point density is the most important when detecting slight ground settlements or elevations. For example, Bollandsås et al. (2012) could show that the lidar-based DTM resolution had a significant effect on the detection success of cultural remains. Especially in densely vegetated areas, enhanced UAV lidar sensors with pulse repetition frequencies beyond 1 MHz and the realization of flight missions with cross-strips could tackle this limiting factor. Another weakness of our methodology for tree species classification is the manual preparation of training and test samples. However, because of understandable reasons, the collection of field reference data was not possible in the study area.

7. Conclusion

Our experiments demonstrated that area-wide detection of unknown radioactive waste sites in the ChEZ can be conducted successfully using the proposed methodology. Overall, we achieved excellent classification results fusing high-resolution UAV-based lidar data and MS imagery. A key factor of our approach is the generation of a feature set that can describe both the ground surface and nearby vegetation. Moreover, we applied an effective feature selection strategy to avoid overfitting of the RF models, resulting in remarkable generalization properties. Furthermore, we presented an efficient correction method for the radiometric data collected by the YellowScan Mapper I laserscanner. Based on geometrically and radiometrically consistent data, precise 3D vegetation mapping at the tree level enabled the generation of meaningful *TF* that supported the proposed classifier. Our results were verified based on 38 borings that confirmed the existence of previously unknown buried nuclear materials in the classified areas. Compared to the ground surface, EDR measurements revealed values up to 30 times greater in the soil layers containing buried biomass and demolition waste. Moreover, it is noteworthy that some of the parameters from 3D vegetation mapping (i.e. tree height, tree species, stem diameters, tree positions) can be used advantageously in radiologic simulations. Based on the results in Briechle et al. (2018), Molitor et al. (2018) calculated the potential exposure to external irradiation from a

single tree species for a person working in the ChEZ forest. Therefore, more realistic radiologic modeling based on the method proposed in this paper for 3D vegetation mapping should be possible. Finally, existing hazard maps could be upgraded using the proposed method to minimize worker radiation dose uptake and optimize accident liquidation.

Declaration of Competing Interest

The authors declare that they have no known competing financial interests or personal relationships that could have appeared to influence the work reported in this paper.

Acknowledgements

The authors would like to thank V. Antropov, O. Tretyak and the collegues from CRWME for the technical support in the ChEZ and the conducted borings. We also highly appreciate the support from Y. Zabulonov from the Institute of Environmental Geochemistry, the supply of the octocopter and its piloting by our Ukrainian colleagues from Flycamstudio. The research was funded by Federal Ministry of Education and Research (BMBF) (Grant No. 03FH004IX6).

References

Agisoft LLC, 2018. Agisoft PhotoScan Professional 1.4.1. https://www.agisoft.com/ (accessed: 2020-05-01).

Amiri, N., Krzystek, P., Heurich, M., Skidmore, A., 2019. Classification of tree species as well as standing dead trees using triple wavelength ALS in a temperate forest. Remote Sens. 11.

Antropov, V., Bugai, D., Dutton, L., Gerchikov, M., Kennett, E., Ledenev, A., Novikov, A., Rudko, V., Ziegenhagen, J., 2001. Review and Analysis of Solid Long-lived and High Level Radioactive Waste arising at the Chernobyl Nuclear Power Plant and the Restricted Zone. Technical Report.

Applied Imagery, 2018. Quick Terrain Modeler v8.0.7. http://www.appliedimagery.com (accessed: 2020-05-01).

Arkhipov, N., Kuchma, N., Askbrant, S., Pasternak, P., Musica, V., 1994. Acute and long-term effects of irradiation on pine (Pinus silvestris) stands post-Chernobyl. Sci. Total Environ. 157, 383–386.

Axelsson, P., 2000. DEM generation from laser scanner data using adaptive TIN models. Int. Arch. Photogram. Remote Sens. Spatial Inform. Sci. ISPRS Arch. 33, 110–117 (accessed: 2020–05-01).

BayesMap Solutions LLC, 2018. BayesStripAlign 2.0. http://bayesmap.com/products/bayesstripalign/ (accessed: 2020-05-01).

Bollandsås, O., Risbøl, O., Ene, L., Nesbakken, A., Gobakken, T., Næsset, E., 2012. Using airborne small-footprint laser scanner data for detection of cultural remains in forests: An experimental study of the effects of pulse density and DTM smoothing. J. Archaeol. Sci. 39, 2733–2743.

Bonzom, J.-M., Hättenschwiler, S., Lecomte-Pradines, C., Chauvet, E., Gaschak, S., Beaugelin-Seiller, K., Della-Vedova, C., Dubourg, N., Maksimenko, A., Garnier-Laplace, J., Adam-Guillermin, C., 2016. Effects of radionuclide contamination on leaf litter decomposition in the Chernobyl Exclusion Zone. Sci. Total Environ. 562, 596–603.

Briechle, S., Sizov, A., Tretyak, O., Antropov, V., Molitor, N., Krzystek, P., 2018. UAV-based detection of unknown radioactive biomass deposits in Chernobyl's Exclusion Zone. Int. Arch. Photogram. Remote Sens. Spatial Inform. Sci. - ISPRS Arch. 42, 163–169.

Bugai, D., Kashparov, V., Dewiére, L., Khomutinin, Y., Levchuk, S., Yoschenko, V., 2005. Characterization of subsurface geometry and radioactivity distribution in the trench containing Chernobyl clean-up wastes. Environ. Geol. 47, 869–881.

Bugai, D., Skalskyy, A., Dzhepo, S., Kubko, Y., Kashparov, V., Van Meir, N., Stammose, D., Simonucci, C., Martin-Garin, A., 2012. Radionuclide migration at experimental polygon at Red Forest waste site in Chernobyl zone. Part 2: Hydrogeological characterization and groundwater transport modeling. Appl. Geochem. 27, 1359–1374.

CloudCompare Development Team, 2019. CloudCompare 2.8 [GPL software]. http://www.cloudcompare.org/ (accessed: 2020-05-01).

Davids, C., Tyler, A., 2003. Detecting contamination-induced tree stress within the Chernobyl Exclusion Zone. Remote Sens. Environ. 85, 30–38.

European Union (2014–2017). Support to radioactive waste management in Ukraine. https://nuclear.jrc.ec.europa.eu/tipins/contracts/support-radioactive-waste-management-ukraine (accessed: 2020-05-01).

Fassnacht, F., Latifi, H., Sterenczak, K., Modzelewska, A., Lefsky, M., Waser, L., Straub, C., Ghosh, A., 2016. Review of studies on tree species classification from remotely sensed data. Remote Sens. Environ. 186, 64–87.

Flynn, K., Glendenin, L., Harkness, A., Steinberg, E., 1965. Half-lives of 90Sr and 137Cs. J. Inorg. Nucl. Chem. 27, 21–23.

Gevaert, C., Persello, C., Nex, F., Vosselman, G., 2018. A deep learning approach to DTM extraction from imagery using rule-based training labels. ISPRS J. Photogram. Remote Sens. 142, 106–123.

Gregorutti, B., Michel, B., Saint-Pierre, P., 2017. Correlation and variable importance in random forests. Stat. Comput. 27, 659–678.

Guyot, A., Hubert-Moy, L., Lorho, T., 2018. Detecting Neolithic burial mounds from lidar-derived elevation data using a multi-scale approach and machine learning techniques. Remote Sens. 10.

Höfle, B., Pfeifer, N., 2007. Correction of laser scanning intensity data: Data and model-driven approaches. ISPRS J. Photogram. Remote Sens. 62, 415–433.

Holmgren, J., Persson, Å., Söderman, U., 2008. Species identification of individual trees by combining high resolution lidar data with multi-spectral images. Int. J. Remote Sens. 29, 1537–1552.

Ibeo Automotive Systems GmbH, 2010. Operating manual ibeo LUX 2010 laserscanner v1.6. Unpublished internal technical report, pp. 20.

Immitzer, M., Atzberger, C., Koukal, T., 2012. Tree species classification with random forest using very high spatial resolution 8-band worldview-2 satellite data. Remote Sens. 4, 2661–2693.

Jalobeanu, A., Gonçalves, G.R., 2014. Automated probabilistic lidar swath registration. In: AGU Fall Meeting Abstracts.

Jutzi, B., Gross, H., 2009. Normalization of lidar intensity data based on range and surface incidence angle. Int. Arch. Photogram. Remote Sens. Spatial Inf. Sci. 38, 213–218 (accessed: 2020–05-01).

Kaasalainen, S., Jaakkola, A., Kaasalainen, M., Krooks, A., Kukko, A., 2011. Analysis of incidence angle and distance effects on terrestrial laser scanner intensity: Search for correction methods. Remote Sens. 3, 2207–2221.

Kaminska, A., Lisiewicz, M., Sterenczak, K., Kraszewski, B., Sadkowski, R., 2018. Species-related single dead tree detection using multi-temporal ALS data and CIR imagery. Remote Sens. Environ. 219, 31–43.

Kashparov, V., Yoschenko, V., Levchuk, S., Bugai, D., Van Meir, N., Simonucci, C., Martin-Garin, A., 2012. Radionuclide migration in the experimental polygon of the Red Forest waste site in the Chernobyl zone - Part 1: Characterization of the waste trench, fuel particle transformation processes in soils, biogenic fluxes and effects on biota. Appl. Geochem. 27, 1348–1358.

Korpela, I., Ørka, H., Hyyppå, J., Heikkinen, V., Tokola, T., 2010. Range and AGC normalization in airborne discrete-return lidar intensity data for forest canopies. ISPRS J. Photogram. Remote Sens. 65, 369–379.

Kuhn, M., 2008. Building predictive models in R using the caret package. J. Stat. Softw. 28, 1–26.

Lasaponara, R., Coluzzi, R., Gizzi, F., Masini, N., 2010. On the lidar contribution for the archaeological and geomorphological study of a deserted medieval village in Southern Italy. J. Geophys. Eng. 7, 155–163.

Latifi, H., Heurich, M., 2019. Multi-scale remote sensing-assisted forest inventory: A glimpse of the state-of-the-art and future prospects. Remote Sens. 11.

Liaw, A., Wiener, M., 2002. Classification and regression by randomforest. R News 2, 18–22 (accessed: 2020–05-01).

Ma, L., Fu, T., Blaschke, T., Li, M., Tiede, D., Zhou, Z., Ma, X., Chen, D., 2017. Evaluation of feature selection methods for object-based land cover mapping of unmanned aerial vehicle imagery using random forest and support vector machine classifiers. ISPRS Int. J. Geo-Inform. 6.

MicaSense Inc, 2015. MicaSense RedEdge 3 Multispectral Camera User Manual, Rev 06. https://support.micasense.com/hc/en-us/article_attachments/204648307/RedEdge_User_Manual_06.pdf (accessed: 2020-05-01).

MicaSense Inc, 2019. Use of calibrated reflectance panels for rededge data. https://support.micasense.com/hc/en-us/articles/115000765514-Use-of-Calibrated-Reflectance-Panels-For-RedEdge-Data (accessed: 2020-05-01).

Molitor, N., Thierfeldt, S., Haneke, K., Nitzsche, O., Bugai, D., Sizov, A., Drace, Z., 2017. Recent safety assessment findings on management of legacy wastes from Chornobyl accident. In: International Conference on Nuclear Decommissioning and Environment Recovery, INUDECO. https://www.researchgate.net/publication/317400817_Recent_safety_assessment_findings_on_management_of_legacy_wastes_from_Chornobyl_accident (accessed: 2020-05-01).

Molitor, N., Zabulonov, Y., Krzystek, P., Siebold, K., Haneke, K., Nitzsche, O., Groot J., d., Antropov, V., Tretyak, O., Sizov, A., Bugai, D., Kovach, V., Bayer, P., Drace, Z., Bachmaier, B. (2018). New developments in airborne geophysical survey technologies and their application for investigation and radiological assessment of highly contaminated areas and legacy radioactive waste storages in the Chornobyl Exclusion Zone. In: International Conference on Nuclear Decommissioning and Environment Recovery, INUDECO. https://www.researchgate.net/publication/327704022_New_developments_in_airborne_geophysical_survey_technologies_and_their_application_for_investigation_and_radiological_assessment_of_highly_contaminated_areas_and_legacy_radioactive_waste_storages_in_t (accessed: 2020-05-01).

Næsset, E., 2004. Practical large-scale forest stand inventory using a small-footprint airborne scanning laser. Scand. J. For. Res. 19, 164–179.

NovAtel Inc., 2017. Inertial Explorer 8.70 - GNSS and inertial post-processing software. https://www.novatel.com/products/software/inertial-explorer/ (accessed: 2020-05-01).

Pal, M., 2005. Random forest classifier for remote sensing classification. Int. J. Remote Sens. 26, 217–222.

Polewski, P., Yao, W., Heurich, M., Krzystek, P., Stilla, U., 2015. Detection of fallen trees in ALS point clouds using a Normalized Cut approach trained by simulation. ISPRS J. Photogram. Remote Sens. 105, 252–271.

PRIMAVISION Technologies GbR, 2017. 3D tree segmentation from point clouds (lidar, DSM) for forest inventory. http://primavision-tec.de/products/prod_tree-finder (accessed 2020-05-01).

Puissant, A., Rougiera, S., Stumpf, A., 2014. Object-oriented mapping of urban trees using random forest classifiers. Int. J. Appl. Earth Obs. Geoinf. 26, 235–245.

Pyysalo, U., Hyyppå, H., 2002. Reconstructing tree crowns from laser scanner data for

feature extraction. Int. Arch. Photogram. Remote Sens. Spatial Inform. Sci. ISPRS Arch. 34 (accessed: 2020–05-01).
QGIS Development Team, 2017. QGIS 2.18.3. https://qgis.org (accessed: 2020-05-01).
R Core Team, 2018. R: A language and environment for statistical computing. R foundation for statistical computing. Vienna, Austria. https://www.R-project.org/ (accessed: 2020-05-01).
Reitberger, J., 2010. 3D-Segmentierung von Einzelbäumen und Baumartenklassifikation aus Daten flugzeuggetragener Full Waveform Laserscanner. Ph.D. thesis Technische. Universität München.
Reitberger, J., Krzystek, P., Stilla, U., 2007. Combined tree segmentation and stem detection using full waveform lidar data. Int. Arch. Photogram. Remote Sens. Spatial Inf. Sci. 36, 332–337 (accessed: 2020–05-01).
Reitberger, J., Krzystek, P., Stilla, U., 2008. 3D segmentation and classification of single trees with full waveform lidar data. Proc. SilviLaser 2008 (8), 17–19.
Reitberger, J., Schnörr, C., Krzystek, P., Stilla, U., 2009. 3D segmentation of single trees exploiting full waveform lidar data. ISPRS J. Photogram. Remote Sens. 64, 561–574.
Ørka, H., Gobakken, T., Næsset, E., Ene, L., Lien, V., 2012. Simultaneously acquired airborne laser scanning and multispectral imagery for individual tree species identification. Can. J. Remote Sens. 38, 125–138.
Rodriguez-Galiano, V., Ghimire, B., Rogan, J., Chica-Olmo, M., Rigol-Sanchez, J., 2012. An assessment of the effectiveness of a random forest classifier for land-cover classification. ISPRS J. Photogram. Remote Sens. 67, 93–104.
Rusu, R.B., Blodow, N., Beetz, M., 2009. Fast point feature histograms (FPFH) for 3D registration. In: IEEE International Conference on Robotics and Automation (ICRA), pp. 3212–3217.
Rusu, R.B., Marton, Z.C., Blodow, N., Beetz, M., 2008. Learning informative point classes for the acquisition of object model maps. In: 2008 10th International Conference on Control, Automation, Robotics and Vision (ICARCV), pp. 643–650.
Saintenoy, A., Courbet, C., Nguyen, L., Léger, E., Bugai, D., 2017. Results from two GPR surveys (2002 and 2015) in the Chernobyl Exclusion Zone. In: 2017 9th International Workshop on Advanced Ground Penetrating Radar (IWAGPR). IEEE, pp. 1–6.
Shi, J., Malik, J., 2000. Normalized cuts and image segmentation. IEEE Trans. Pattern Anal. Mach. Intell. 22, 888–905.
Shi, Y., Skidmore, A., Wang, T., Holzwarth, S., Heiden, U., Pinnel, N., Zhu, X., Heurich, M., 2018a. Tree species classification using plant functional traits from lidar and hyperspectral data. Int. J. Appl. Earth Obs. Geoinf. 73, 207–219.
Shi, Y., Wang, T., Skidmore, A., Heurich, M., 2018b. Important lidar metrics for discriminating forest tree species in Central Europe. ISPRS J. Photogram. Remote Sens. 137, 163–174.
Sims, D.A., Gamon, J.A., 2002. Relationships between leaf pigment content and spectral reflectance across a wide range of species, leaf structures and developmental stages. Remote Sens. Environ. 81, 337–354.
Sithole, G., Vosselman, G., 2004. Experimental comparison of filter algorithms for bare-earth extraction from airborne laser scanning point clouds. ISPRS J. Photogram. Remote Sens. 59, 85–101.
Soininen, A., 2016. TerraScan user's guide. https://www.terrasolid.com/download/tscan.pdf (accessed: 2020-05-01).
Solberg, S., Naesset, E., Bollandsas, O., 2006. Single tree segmentation using airborne laser scanner data in a structurally heterogeneous spruce forest. Photogram. Eng. Remote Sens. 72, 1369–1378.
Thiry, Y., Colle, C., Yoschenko, V., Levchuk, S., Van Hees, M., Hurtevent, P., Kashparov, V., 2009. Impact of Scots pine (Pinus sylvestris L.) plantings on long term 137Cs and 90Sr recycling from a waste burial site in the Chernobyl Red Forest. J. Environ. Radioact. 100, 1062–1068.
Tikhomirov, F., Shcheglov, A., 1994. Main investigation results on the forest radioecology in the Kyshtym and Chernobyl accident zones. Sci. Total Environ. 157, 45–57.
Trier, Ø.D., Salberg, A.-B., Kermit, M., Rudjord, Ø., Gobakken, T., Næsset, E., Aarsten, D., 2018. Tree species classification in Norway from airborne hyperspectral and airborne laser scanning data. Eur. J. Remote Sens. 51, 336–351.
Usoltsev, V., Shobairi, S., Chasovskikh, V., 2019. Comparing of allometric models of single-tree biomass intended for airborne laser sensing and terrestrial taxation of carbon pool in the forests of Eurasia. Nat. Resource Model. 32.
Ussyshkin, R., Ravi, R., Ilnicki, M., Pokorny, M., 2009. Mitigating the impact of the laser footprint size on airborne lidar data accuracy. In: American Society for Photogrammetry and Remote Sensing Annual Conference 2009 (ASPRS), vol. 2, pp. 854–862 (accessed: 2020-05-01).
Wu, B., Yu, B., Wu, Q., Huang, Y., Chen, Z., Wu, J., 2016. Individual tree crown delineation using localized contour tree method and airborne lidar data in coniferous forests. Int. J. Appl. Earth Obs. Geoinf. 52, 82–94.
YellowScan, 2016. YellowScan Mapper - The lightweight LiDAR solution for UAVs. https://www.microgeo.it/public/userfiles/Yellowscan-Mapper-datasheet.pdf (accessed: 2020-05-01).
Yoschenko, V., Kashparov, V., Melnychuk, M., Levchuk, S., Bondar, Y., Lazarev, M., Yoschenko, M., Farfán, E., Jannik, G., 2011. Chronic irradiation of Scots pine trees (Pinus Sylvestris) in the Chernobyl Exclusion Zone: Dosimetry and radiobiological effects. Health Phys. 101, 393–408.
Yu, X., Hyyppä, J., Litkey, P., Kaartinen, H., Vastaranta, M., Holopainen, M., 2017. Single-sensor solution to tree species classification using multispectral airborne laser scanning. Remote Sens. 9.
Zabulonov, Y., Burtnyak, V., Zolkin, I., 2015. Airborne gamma spectrometric survey in the Chernobyl exclusion zone based on oktokopter UAV type. Problems Atom. Sci. Technol. 99, 163–167 (accessed: 2020–05-01).